WINTERTIME TURBULENCE AND MIXING ON THE CENTRAL ISRAELI SHELF

A Thesis

by

CHENXI MA

Submitted to the Graduate and Professional School of
Texas A&M University
in partial fulfillment of the requirements for the degree of

MASTER OF SCIENCE

Chair of Committee,	Ayal Anis
Committee Members,	Karl Kaiser Hui Liu
Head of Department,	Shari Yvon-Lewis

May 2022

Major Subject: Oceanography

ABSTRACT

The purpose of this study is to describe turbulent mixing processes on the Israel Shelf in the winter season as well as the physical mechanisms driving the mixing events. Data for the study has been collected during two scientific cruises on board the R/V Shikmona and will be based mainly on vertical casts made with the state-of the art turbulence profilers. Ancillary data was provided from coastal meteorology stations and the reanalysis data from the ECMWF (European Centre for Medium-Range Weather Forecasts) providing surface meteorological parameters from which surface forcing was estimated (surface wind stress and buoyancy fluxes). As far as we know, in this very region, no previous turbulence data has been collected and/or published in the open literature.

The results indicate that in the winter of Israeli Shelf, the mixing event is mainly driven by buoyancy fluxes (J_b^0), the dissipation rate of turbulent kinetic energy (ϵ) and Jb0 share a similar order of magnitude, around 10^{-7} W/kg. The ϵ / J_b^0 were calculated and plotted against z/D, the depth over the mixing layer depth to obtain a general distribution of ϵ. This study can provide insight to the construction of turbulent models, and thus may further help the study in other oceanography field.

ACKNOWLEDGEMENTS

I would like to thank my committee chair, Dr. Anis, and my committee members, Dr. Liu, Dr. Kaiser, for their guidance and support throughout the course of this research.

Thanks also go to my friends and colleagues and the department faculty and staff for making my time at Texas A&M University a great experience.

Thanks also to my parents in China who support my study in Texas A&M University, and give me courage in my study through the pandemic.

TABLE OF CONTENTS

Page

LIST OF FIGURES

Page

LIST OF TABLES

Page

1. INTRODUCTION

Turbulent mixing has an important influence on the vertical transport of mass and energy. The transport of mass, such as nutrients, tracers, or pollutants have great influence in chemical and biological oceanographic processes, like the growth of phytoplankton, the variation of a chemical compound in concentration. The transport of energy mainly heat, has a major influence on the heat budget and climate regulation. Therefore, in a wide variety of aspects, many studies are conducted on turbulent mixing in order to understand the mechanisms within.

According to Herut (2000) research with 12 cruises over 2 years was conducted along the Israeli Shelf with R/V Shikmona, the same general region in which this study has been conducted. The results from the CTD and sampled nutrients' concentrations showed that during winter the water column in this region is well mixed from the surface to a depth of about 150 meters, which leads to an input of nutrients from the deep layers into the euphotic zone, and further causes phytoplankton blooms during winter.

Also, according to Jurado (2007), a 1-D model coupling dynamic and hydrodynamic-contaminate was developed to simulate the persistence of organic pollutants (POP) status in a Mediterranean continental shelf environment, the Adriatic Sea. The results from that study demonstrate that turbulent mixing played an important role in the POP concentration.

These two studies looked into the impact of turbulent mixing to the marine environment, especially in vertical transport of matters. Meanwhile, a lot of studies

focused deeper into one of the properties of the turbulence, the dissipation rate. Within the water column, when the flow became more turbulent due to the build up of shear instability, energy will be transformed from large scale eddies to smaller structures, and eventually dissipated into heat irreversibly. As a result, the study of dissipation rate is important to the understanding of turbulent mixing.

Thiébaut et al. (2020) used two coupled ADCP to measure the budget of turbulent kinetic energy in Alderney Race, including the production rate (P) and the dissipation rate (ϵ). Turbulence in that region was generated by tidal influence, the ration of the dissipation rate over the production rate (ϵ/P) is 2.2 during the flood and 2.8 during the ebb, and the power spectrum density on velocity also demonstrate different patterns.

Wiles et al. (2006) applied a new technique in measuring the dissipation rate of turbulent kinetic energy from ADCP velocity data collected in Red Wharf Bay. The method was adapted from the structure function in radar meteorology, and compared with data from a Fast-Light-Yoyo (FLY) microstructure profiler. The ratio between these two methods is around 0.68±0.23, due to the lack of noise estimation.

Klein et al. (1981) applied a 1D simplified model, which is similar to Mellor-Yamada 3 model, to study the surface mixing layer and the thermocline depth under different types of environments. According to this study, wind stress and surface heat flux have an important impact on the turbulent kinetic energy diffusion and temporary and spatial variation, whereas the wave breaking is not as effective as wind condition and heat budget.

Peters et al. (2000) observed the turbulent mixing in both the water column and the bottom boundary layer of Hudson River estuary during 1995 summer and fall. The turbulent mixing condition is affected by the stratification from fresh water discharge, the mixing done by the tides, and some local atmospheric forcing. The result from the study shows that the dissipation rate can reach to a maximum of 10-4 W/kg during spring ebbs, the depth integrated dissipation rate is correlated to the tidal pressure gradient forcing, and the dissipation rate also indicate the local shear instability is an important source of turbulent generation.

1.1 Background Information Relevant to the Study Area

The Israeli Shelf is located in the east to south-east margin of Mediterranean Sea (fig.1). The bathymetry of the shelf is north-south in general, roughly parallel to the coastline. The coastline of the Israeli shelf and the Egyptian Sinai coast form a right angle in the south. However, compared to the Sinai coast, the Israeli Shelf is relatively narrow, which means that it reaches the deep sea after a relatively short distance. A steep continental slope links the Israeli shelf with a semi-enclosed basin, the Levantine Basin. The Levantine Basin shares the same sub-tropical climate as the Mediterranean Sea and is characterized by cool and rainy weather in winter (November to March), and hot and rather dry weather in the summer (May to September) (Abudaya, 2013).

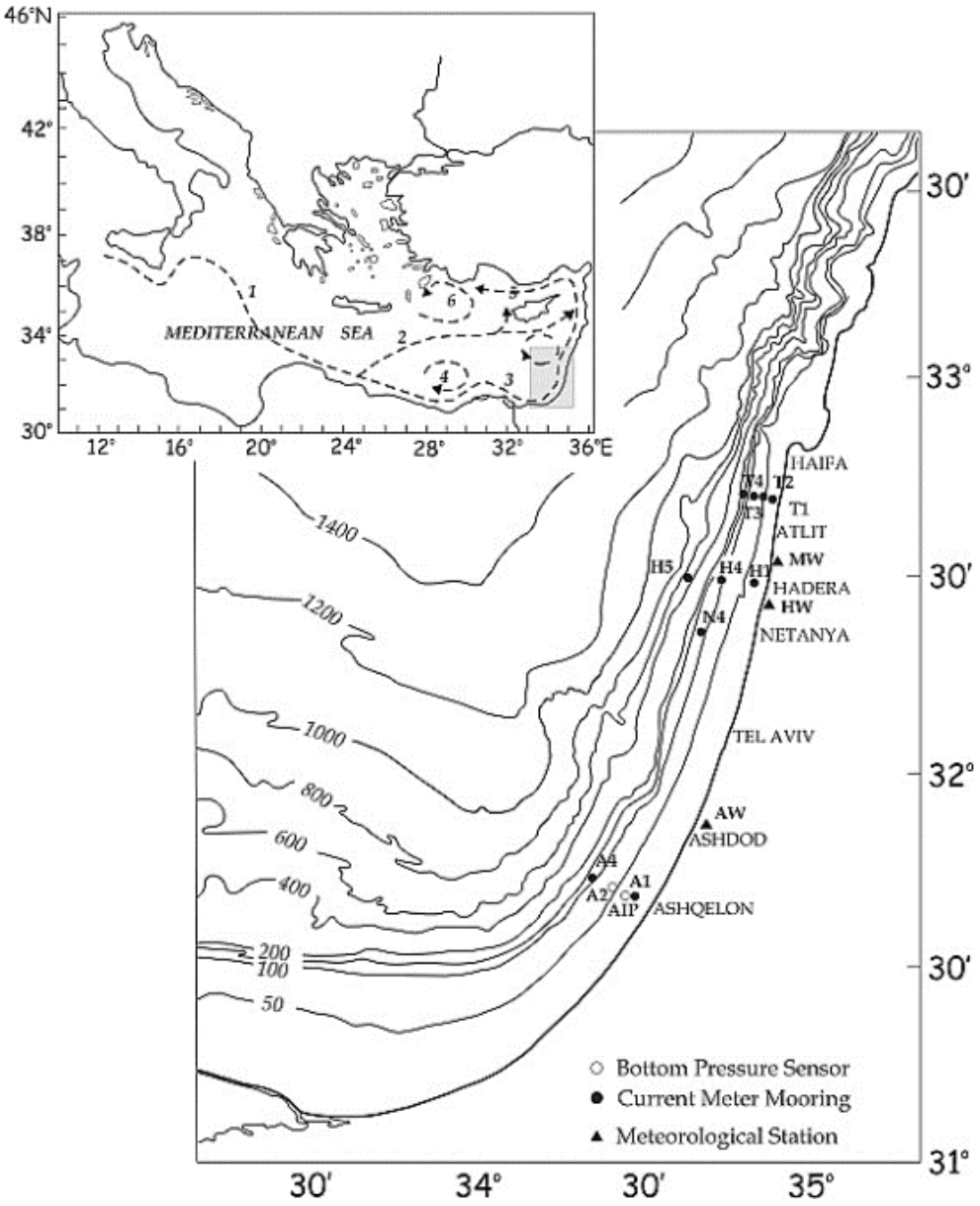

Figure 1.1 Location of the Israeli Shelf and its bathymetry. Reprinted from figure 1 in (Rosentraub et al., 2007)

1.2 South Levantine Basin

According to Robinson (1992), the currents in the south-east Mediterranean Sea are dominated by the Mid-Mediterranean Jet (MMJ) along the Israeli shelf and the

Shikmona Gyre (fig 2.) on its west. The MMJ flows southward, and the Shikmona Gyre presents a clockwise pattern. Abudaya (2013) used the yearly averaged sea surface temperature (SST) data to study the area, and therefore the reported southward MMJ and clockwise pattern of Shikmona Gyre likely represent the overall trend albeit without the seasonal variability.

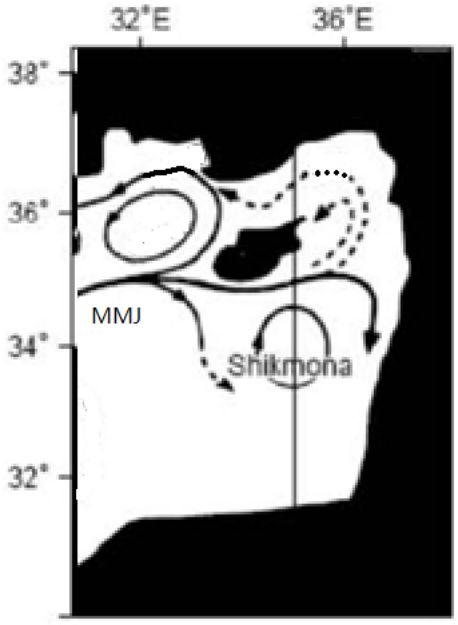

Figure 1.2 The diagram of major currents in the eastern Mediterranean. Adapted from Figure 8 in (Abudaya, 2013)

The seasonal variability of the MMJ and Shikmona Gyre, which is induced by seasonal changes in the wind pattern, has been discussed in Malanotte-Rizzoli (1988). During summer, the Shikmona Gyre presents a counter-clockwise trend and the MMJ flows northward on its east along the Israeli shelf. However, in the winter, the MMJ crosses the Shikmona Gyre from west toward the north, and thus the Israeli shelf is

dominated by a southward current from the eastern part of the clockwise Shikmona Gyre. (fig. 3)

Figure 1.3 Transport stream function in $10^9 cm^3 s^{-1}$: a) winter; b) summer Adapted from (Menzin & Moskalenko, 1982).

1.3 The Israeli Shelf

Compared to the South Levantine Basin, the currents on the shelf are mainly following the same direction as wind stress. In general, the velocity of the wind and the currents are northward alongshore, especially during the winter and summer. Only in April and September, which are transition months, the wind stress and current velocity point southward. During winter, surface water tends to be driven in an onshore direction by the Ekman transport brought by the strong northward winds. The downwelling Ekman pumping caused by the onshore transport leads to a deep thermocline, which has been found around a depth of 250 meters in this study. A downward offshore flux of denser shelf water on the slope has been reported to enhance the cross-shelf transport processes on the narrow Israeli Shelf (Rosentraub et al., 2007) (fig. 1.4).

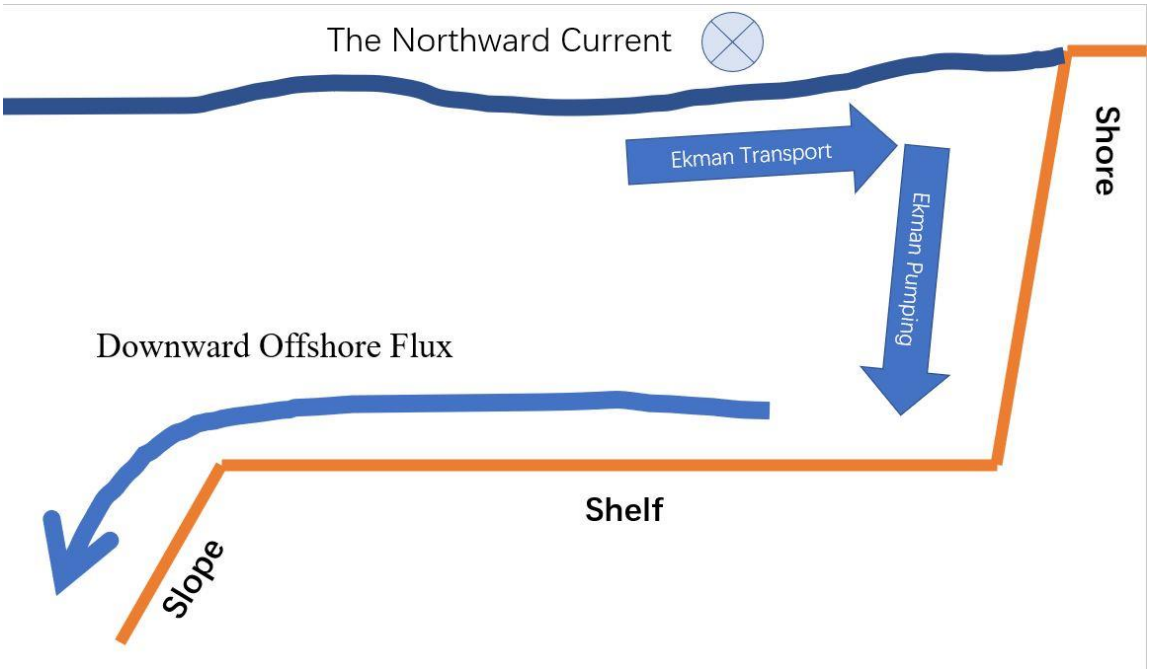

Figure 1.4 The diagram demonstrates the vertical circulation on the Israel Shelf, which is based on the description of Rosentraub (2007)

The deep mixing layer in winter on the narrow shelf can be viewed as a combination of both surface forcing, including surface cooling and wind stress, and the geostrophic circulation (Robinson et al., 1991). In order to elucidate the major processes driving this unique mixing phenomena, both the mixing dynamics of the water column and the wind climate which provides the major surface forcing needs to be assessed.

1.4 Study Objectives

This study has three main objectives:

(1) Estimate the TKE dissipation rates in the observational region of the Israeli shelf by using a spectrum fitting method (Nasmyth 1970),

(2) Discuss the winter forcing regime by applying meteorological data from ECMWF (European Centre for Medium-Range Weather Forecasts) and coastal meteorological stations**.**

(3) Elucidate the role of surface forcing in this unique mixing phenomena.

The study is constructed as follows: section 2 describes the methodology of this study, including the hydrographic data sources, processing of meteorological data, spectral estimates of the microstructure velocity shear, and the estimation of TKE dissipation rates. Section 3 presents the results and is followed by a discussion in Section 4, and section 5 summarizes the main results and suggests additional future work.

2. METHODS

2.1 Data sources

The data for this turbulence study was acquired during two trips in the central Israeli Shelf (fig 2.1) conducted in 2009 January 6^{th}-9^{th} and 18^{th}-21^{st} by Z. Rosentraub (IOLR, Israel) and A. Anis (Texas A&M University, USA). In total, 216 profiles in trip 1 were mostly sampled around 32.5 N 34.7 E, with a bottom depth ranging from 200 meters to about 300 meters. For trip 2, the profiles were sampled around 32.5 N, and from 34.65 to 34.85 E, and totaled 658 profiles. The bottom depth of trip 2 profiles increases when moving west, from 50 meters close to the coast line to 300 meters at the western reach of the transects. The datasets include the following parameters: temperature, conductivity, pressure, micro-temperature, micro-conductivity, microscale velocity shears in two perpendicular directions, profiler acceleration, turbidity, and chlorophyll a. Micro-temperature and micro-conductivity sensors are more sensitive than the "regular" respective sensors, allowing them to record smaller and more rapid changes. All sensors were mounted at the nose of a MSS profiler, a tethered, free-falling profiler, which sank at a stable speed of about 0.7 m/s and was recovered with a ship mounted winch, after the profiler reached the bottom. (fig 2.2)

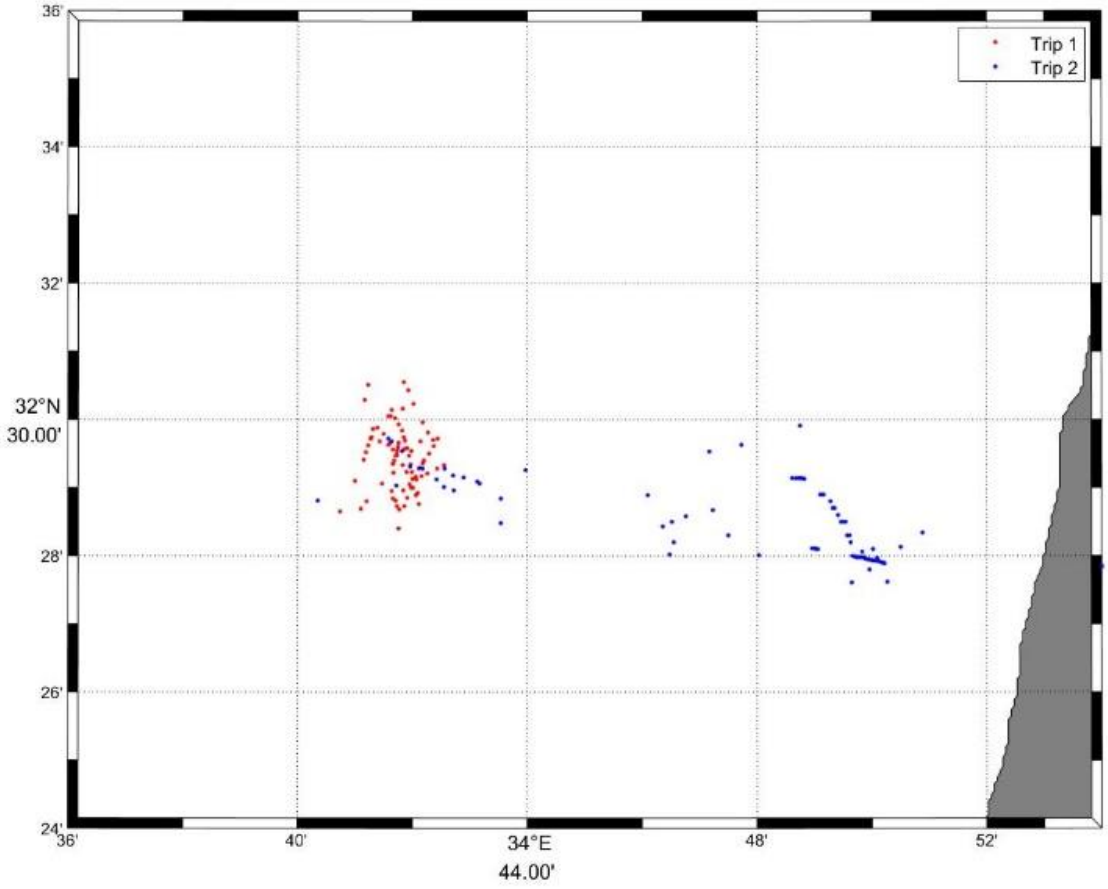

Figure 2.1 Sampling locations of trip 1 (red dots) and trip 2 (blue dots).


WATER TAXI

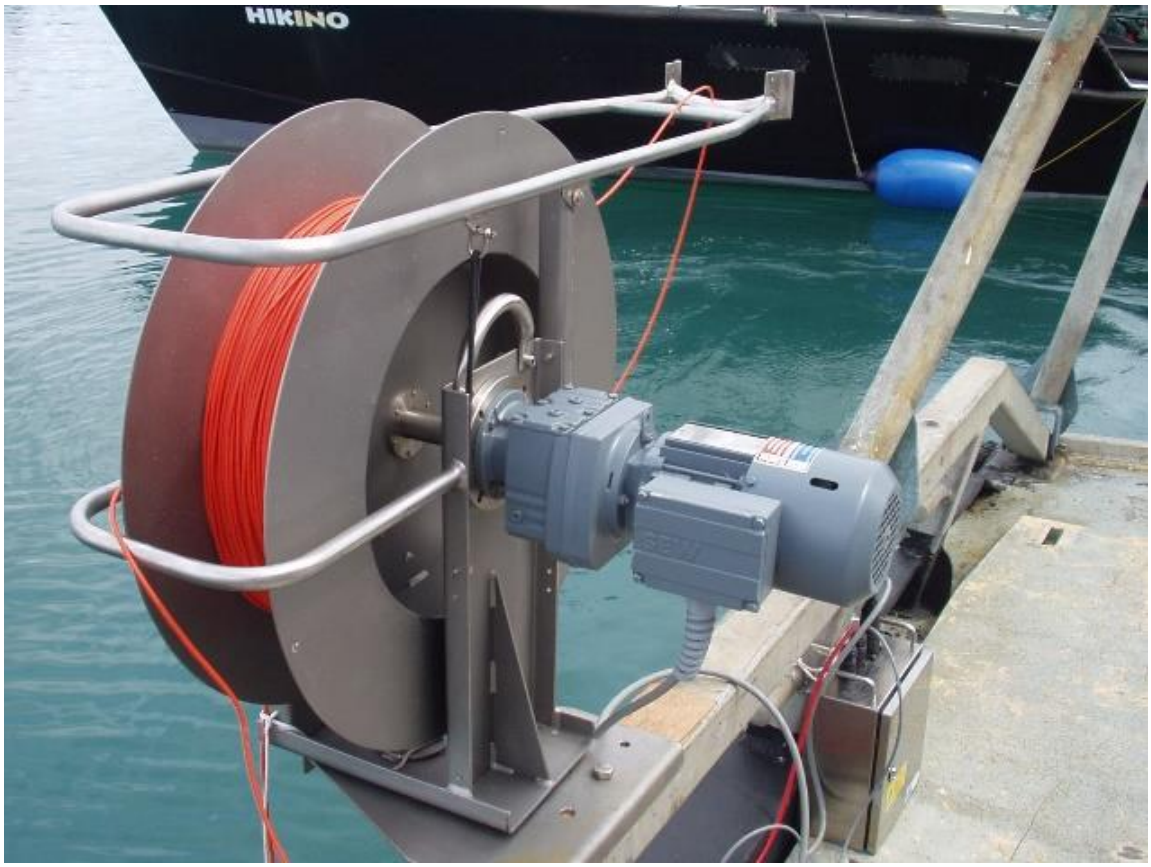

Figure 2.2 The sensors on the profiler (top) and the ship mounted winch (bottom).

The following details about the sensors were obtained from the MSS90 user's manual:

Pressure sensor P

Principle: temperature compensated piezoresistive full bridge

Ranges 10, 20, 50, 100, 200 Bar

Resolution 0.002% FS

Accuracy: 0.1% FS

Response time 150ms

Precision temperature sensor T

Principle: linearized Wheatstone bridge with PT 100

Range -2 … 36°C

Resolution 0,0006°C

Accuracy +/-0.01°C

Response time 150 ms at 1 m/s flow

Precision conductivity sensor C

Principle: symmetrical cell with 7 electrodes

Ranges 0 … 60, 0 … 6 mS/cm

Resolution 0.001 mS/cm, 0,0001 mS/cm

Accuracy +/-0.02 mS/cm, +/- 0,005 mS/cm

Response time 150 ms

Turbidity TURB

Principle: optical back scattering 90°

Range: 0 ... 25, 125, 500, 2500 FTU

Resolution: 0,01 %

Accuracy: 2%

Response time 100 ms

Fluorescence sensor FLU

Principle: optical back scattering 90°

Range: 0 ... 50µg/L Chl a,

Resolution: 0,01 %

Accuracy: 1%

Response time 100 ms

Microstructure temperature sensor NTC

Principle: NTC-resistor electronically linearized

Range: -2 ... 32°C

Resolution: 0,0005°C

Accuracy: +/- 0,02°C

Response time 12 ms at 1 m/s flow

Microstructure current shear sensor SHE

Principle: piezoceramic bending element

Range 0 … 6 1/s (10^{-11} … 10^{-2} W/kg kinetic energy dissipation [dependent on measurements conditions])

Resolution: approx. 10^{-3} 1/s

Accuracy: not specified

Response time: approx. 4 ms

Acceleration sensor ACC

Principle: piezoceramic bending element

Range: 0 … 3 m/sec^2

Resolution: 0,005 m/sec^2

Accuracy: 0,02 m/sec^2

Response time: approx. 4 ms

Microstructure conductivity Cm

Principle: capillary cell two electrodes

Range: 0…60 mS/cm

Resolution: 1µS/cm

Accuracy: 0,5 mS/cm

Response time: approx. 5 ms

2.2 Surface meteorology

Meteorological data was obtained from ECMWF (European Centre for Medium-Range Weather Forecasts) and the meteorology stations including to estimate the impact of the wind and buoyancy fluxes on the turbulent mixing. There are two major meteorological surface processes that may contribute to turbulent mixing: 1. Loss of heat and buoyancy during night or cold air outbreaks and 2. the mechanical induced mixing from the wind stress. Loosing heat at the surface tends to increase the surface density, increasing the instability of the water column, leading to so convective produced

turbulent mixing. Wind stress tends to increase the water current shear near the surface, and increase turbulent mixing through shear forcing.

2.2.1 Surface buoyancy flux

Direct heat loss, J_q^0, was computed by summing surface sensible heat flux J_q^s (Eq. 1), surface latent heat flux J_q^e, short wave radiation J_q^{sw}, and long wave radiation J_q^{lw}(units of W/m^2). The buoyancy flux, J_b^0, was calculated by using the following formulation (Anis et al., 2006), where g is the acceleration of gravity, ρ_w is the surface seawater density, α is the thermal expansion coefficient, β_S is the haline contraction and C_p is the specific heat capacity of seawater:

$$\begin{cases} J_q^0 = J_q^{sw} + J_q^{lw} + J_q^s + J_q^e \\ J_b^0 = \frac{g}{\rho_w}\left(\frac{\alpha}{C_p}J_q^0 + \frac{\beta s}{L_E(1-s)}J_q^e\right) \end{cases} \quad (1)$$

2.2.2 Surface Wind Stress

Surface wind stress is calculated from $\tau = \rho_a C_d {u_{10}}^2$, where ρ_a is the air density, about 1.29 kg/m^3, C_d is the drag coefficient and u_{10} is the wind velocity at 10-meter above the sea-surface. In order to compare the relative contributions of the surface wind stress, and surface buoyancy flux J_b^0, the Monin–Obukhov (M-O) length scale, L was calculated. Here, u_*, (units of m/s), is the water surface friction velocity computed from the wind stress and water density, κ is Karman's constant, about 0.41.

$$u_* = \sqrt{\frac{\tau}{\rho}} \quad (2)$$

$$L = \frac{-{u_*}^3}{\kappa J_b^0} \quad (3)$$

2.3 Hydrographic data

Temperature and salinity data were converted from raw binary data to engineering units, ℃ and PSU, respectively. Density was calculated using Matlab's seawater tool box. The buoyancy frequency, N^2, which provides a measure of the stability of the water column, was calculated from the following formula (in s^{-2}):

$$N^2 = \frac{-g}{\rho}\frac{d\rho}{dz} \quad (4)$$

Before we calculated salinity, a salinity correction was needed. The temperature sensor and the conductivity sensor are slightly displaced from each other on the profiler and their response time is not the same as well. As a result, this creates a lag in the data from the two sensors and which was corrected by lagging the temperature sensor 150 data points in respect to the conductivity data. By setting different gap values, and calculating the salinity, the best lag (150 points) was found upon minimizing salinity spiking.

2.4 Turbulent Kinetic Energy

Turbulent flows (e.g. Lueck, 2013) can be characterized as a chaotic, rotational, dissipative, and diffusive flows. With the combination of vortex–vortex interaction and pressure–velocity correlations, large scale eddies are broken into small scale eddies. This non-dissipative motion also passes turbulent kinetic energy (TKE) from the larger eddies

down to smaller scale eddies. When the scale of these eddies is small enough, the velocity fluctuations will dissipate their kinetic energy via friction at close to molecular scales, turning their energy into heat irreversibly. In order to estimate this energy transfer, the power spectrum method, which expresses the amount of turbulent energy at different wave numbers, is usually utilized. The dissipation rate can thus be estimated by the following equation:

$$\epsilon = \frac{15}{2}\nu\overline{\left(\frac{\partial u}{\partial z}\right)^2} = \frac{15}{2}\nu\int_0^\infty \psi(k)dk \qquad (5)$$

Here, ϵ stands for the dissipation rate of TKE, v is the viscosity of the water, and $\psi(k)$ is the spectrum of the shear $\frac{\partial u}{\partial z}$ at different wavenumbers, k.

2.4.1 Kolmogorov scale

The transfer of energy from large scale background eddies to small scale turbulent fluctuating eddies due to flow instability is referred to as dissipation. After assuming that dissipation occurs at much smaller scales than the largest turbulence scales, Kolmogorov was the first to use the power spectrum of the turbulent velocity fluctuations to describe it. Kolmogorov found that the velocity spectrum is proportional to $k^{-5/3}$, among the wavenumber less than 10-100 cpm (fig 2.3). The kinetic energy per unit mass per unit wavenumber bandwidth, the 'spectral kinetic energy density' can thus be described in the wavenumber range less than 10-100 cpm by:

$$\Phi(k) = q\varepsilon^{\frac{2}{3}}k^{\frac{-5}{3}} \quad (6)$$

$\mathcal{E}$ is the TKE dissipation rate, and q is a constant, about 0.5 (S. A. Thorpe, 2007, An Introduction to Ocean Turbulence).

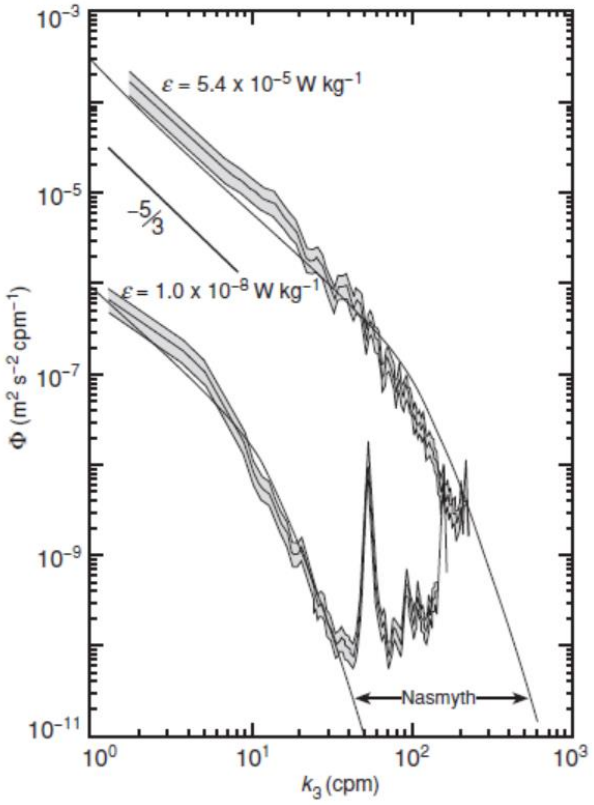

Figure 2.3 Two energy spectra demonstrating the Kolmogorov −5/3 law relationship between 2-6 cpm for the lower spectrum and 2-50 cpm for the upper spectrum, here (S. A. Thorpe, 2007, An Introduction to Ocean Turbulence).

2.4.2 Nasmyth spectrum

However, Kolmogorov -5/3 spectrum cannot predict the dissipation when the scale is large enough to be affected by viscosity (i.e., in fig 2.3, over 6 cpm for the lower spectra and 55 cpm for the upper spectra). Nasmyth (Nasmyth, 1970) derived an empirical spectrum for microstructure velocity shear, the parameter actually measured by the sensors on the turbulence profiler used for this study to express the energy

transfer. The major difference between the Nasmyth spectrum and the Kolmogorov spectrum is that the Nasmyth spectrum is based on velocity shear (du/dz), and the Kolmogorov spectrum is based on velocity only. The Nasmyth spectrum was tabulated at 13 different non-dimensional wavenumbers (Lueck, 2016). An example of this spectrum, taken from Oakey et al. (1981), is shown in Fig 2.4.

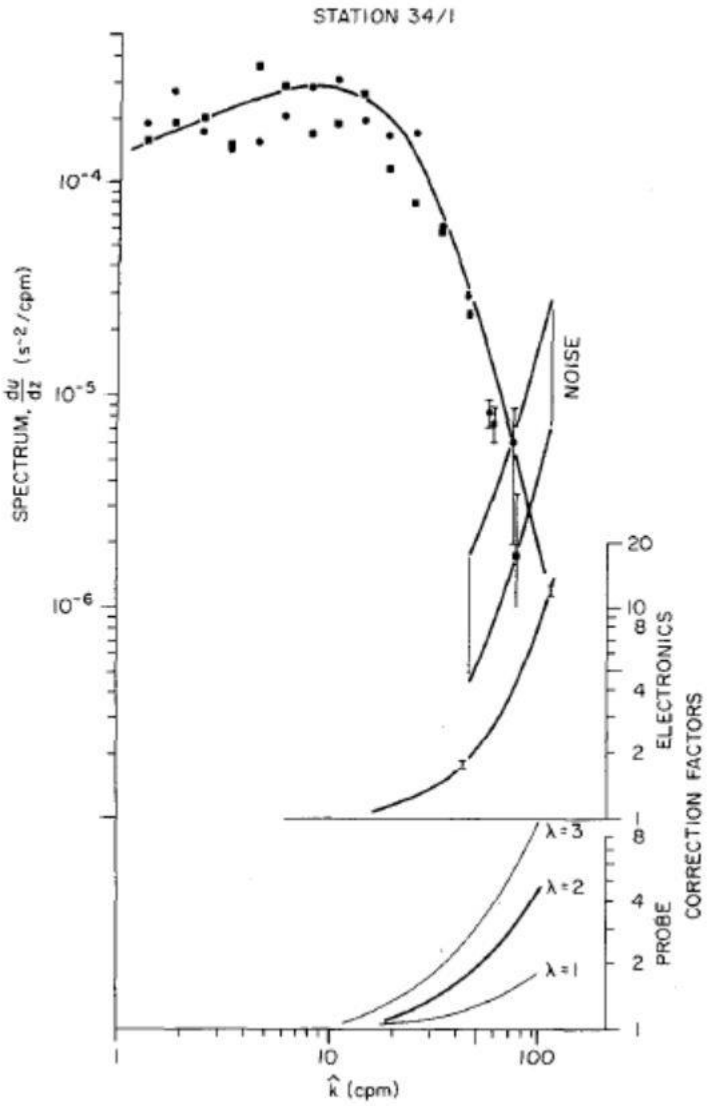

Figure 2.4 The Nasmyth empirical spectrum. (Figure taken from Oakey et al, 1981, Fig. 4) (© American Meteorological Society**)**

Nasmyth spectrum has been used in various studies in estimating the TKE dissipation rate. According to Oakey (1981), the spectrum of temperature gradient and velocity shear has been applied in the study of turbulence to calculate the universal constant q, and the turbulence kinetic energy (TKE) dissipation rate, Ɛ. Also, according to Macoun (2002), this method was mentioned and the impact made by the shape of the probe, the sensor to measure the velocity shear, was fully discussed. In both studies the Nasmyth curve fitting method (Nasmyth, 1970) was applied in calculating the TKE dissipation rate, Ɛ, which provides a measure of the intensity of the turbulent mixing. Similar studies have also been conducted on the Western Mediterranean Sea (Forryan et al., 2012), where the spectrum of shear velocity with over a 1-second window was used to calculate the kinetic dissipation rate through the Nasmyth curve fitting method (Nasmyth, 1970) (fig 10.).

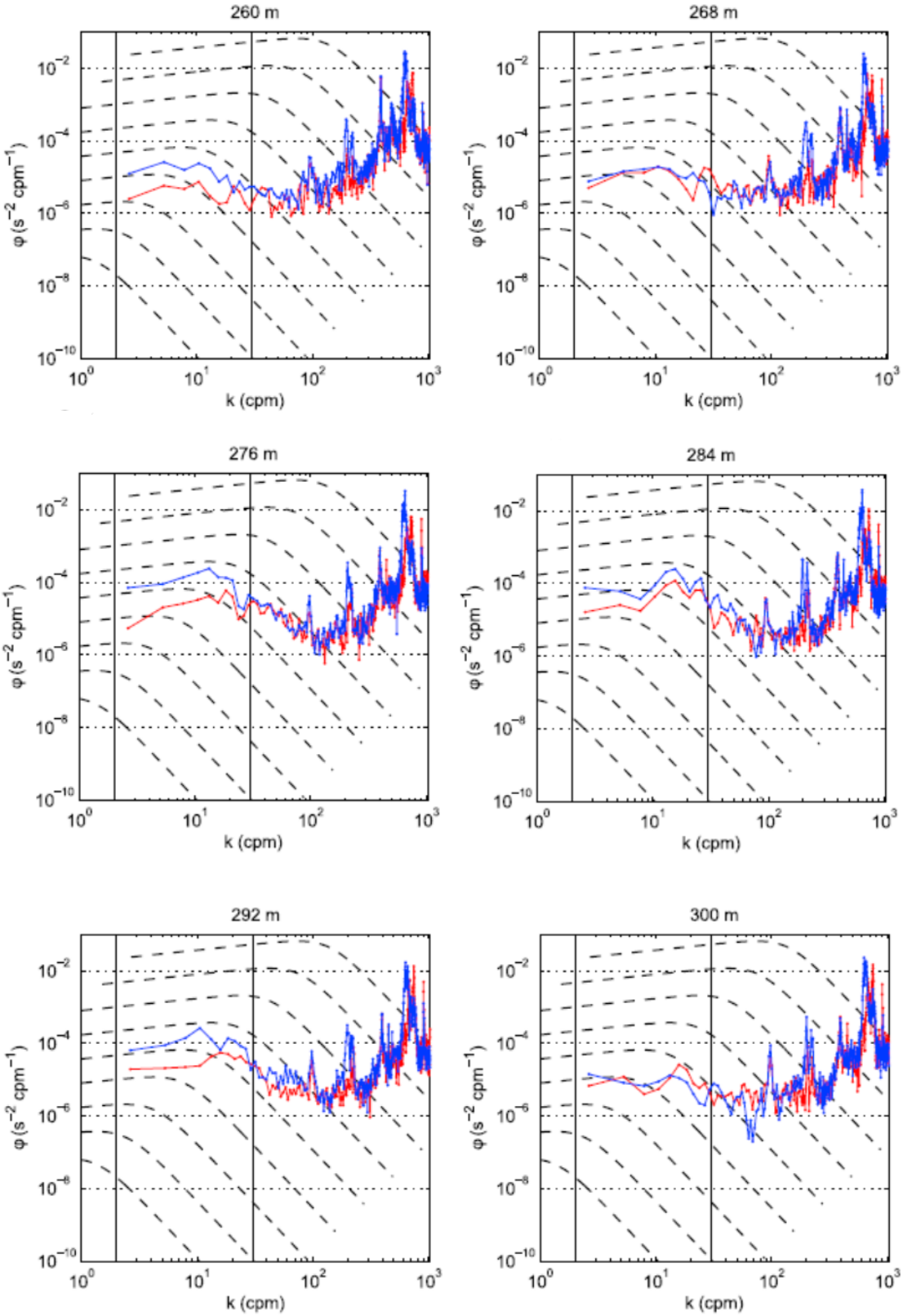
260 m
268 m
276 m
284 m
292 m
300 m
φ (s^{-2} cpm^{-1})
k (cpm)
10^{-2}
10^{-4}
10^{-6}
10^{-8}
10^{-10}
10^{0}
10^{1}
10^{2}
10^{3}

Figure 2.5 Examples of shear velocity spectrum different depths (260 m, 268 m, 276 m, 284 m, 292 m, 300 m) computed over a vertical depth bin of ~1 meter. (Forryan et al., 2012).

2.5 Dissipation rate estimates

Spectral estimation method is used in calculating the dissipation rate $\mathcal{E}$ (units of W/kg). The first step is to remove possible contamination from the acceleration of the profiler, by removing shear probe signals that are coherent with signals from the instrument's accelerometers.

Before we calculate the dissipation rate, we need to divide the water column into bins with statistical steadiness, roughly 1~ 2 meters vertical bins. For each bin, we assume that the Taylor hypothesis holds, which means the advection at this point is mainly caused by the mean flow, and calculate the fall speed of the turbulence profiler from linear regression of depth (estimated from the pressure sensor using the hydrostatic equation) vs time. This is done for each depth bin, Δz:

$$v_{fall} = \frac{\Delta z}{\Delta t} \qquad (7)$$

Shear data is measured by 2 shear sensors, perpendicularly oriented to each other measuring the vertical gradient (shear) of current the two velocity perpendicular components while the tethered instrument is free falling through the water column. At the end of a cast the instrument is pulled back to the surface using a small electrical winch. Within each bin, the Welch spectral method (Welch 1967) was applied to calculate the power spectral density (PSD) of the microstructure velocity shear as a function of frequency, *f*. Conversion from frequency, *f*, to wavenumber space, *k*, can be

determined from the falling speed, and the spectrum density can then be converted from frequency (s^{-1}) to wavenumber space(m^{-1}).

$$\begin{cases} k = \frac{f}{v_{fall}} \\ spd(k) = spd(f) * v_{fall} \end{cases} \quad (8)$$

The Nasmyth empirical curve is then fitted to the observed wavenumber spectrum to provide estimates of the TKE dissipation rate from the best fit (fig 2.4, 2.5). Viscosity of the water (required from computation of $\mathcal{E}$) is calculated from temperature, salinity, and pressure through a Matlab function. For each bin, we assume that the viscosity is homogeneous and the viscosity is then calculated from the average of temperature, salinity, and pressure of data points within the bin.

In this study, three different fitting methods were applied: the "Lueck" method (Lueck 2013), the Stips (Stips et al., 2000) method, and the maximum likelihood estimation (MLE, Ruddick et al., 2000) method. According to Lueck (2013), ϵ_{10}, the integral of the spectrum, $\psi(k)$, with a finite wavenumber interval (0~10 cpm), is used in estimating the dissipation rate ϵ.

$$\begin{cases} \epsilon_{10} = \frac{15}{2}\nu \int_0^{10} \psi(k)dk \\ \frac{\epsilon}{\epsilon_{10}} = \sqrt{1 + a\epsilon_{10}} \end{cases} \quad (9)$$

Here, a is a constant 1.0774×10^9 kgW^{-1}, and ν is the viscosity of the water, which was obtained from pressure, temperature, and salinity, as explained above.

In Stips et al. (2000), ϵ is calculated through the iteration of two equations:

$$\begin{cases} \epsilon = \frac{15}{2}\nu \int_{k_l}^{k_c} \psi(k)dk \ (10.1) \\ k_c = \frac{1}{2\pi}\left(\frac{\epsilon}{\nu^3}\right)^{\frac{1}{4}} (10.2) \end{cases} \quad (10)$$

Here, k_c is the Kolmogorov wavenumber, the upper cut-off wavenumber, and k_l is the lower cut-off wavenumber, set to 2cpm. The dissipation rate, ϵ was calculated by Eq 10.1 through the integration of the spectrum, $\psi(k)$ between k_l and k_c, where k_c was evaluated by Eq 10.2. The final dissipation rate, ϵ was taken as the value when the difference between the new k_c and the previous one was either less than 2 cpm, or k_c was larger than 200 cpm.

The maximum likelihood estimation is a statistic method, widely used in several areas with data following Gaussian distributions. In this case, the most likely value of ϵ, was found by minimizing the following cost function (Ruddick et al., 2000):

$$C_{11} \cong -\sum_{i=1}^{N}\left(\frac{S_{obs}-S_{th}}{S_{th}}\right)^2 - \sum_{i=1}^{N} ln(S_{th}) + N\left(\frac{1}{4}+\sqrt{\frac{d}{4\pi}}\right) \qquad (11)$$

Here, S_{obs} and S_{th} are spectra of the observational data and theoretical Nasmyth curve, respectively, at different wave number. The degrees of freedom, d is a constant (8/3 in this case) dependent on the window used (Hanning window). N is the total number of wave numbers. The likelihood function is close to the Gaussian distribution, and thus the upper and lower ϵ with 95% confidence can be found through bootstrap method（Efron et al., 1983）. The main step for bootstrap method is resampling the current data for multiple times, by doing this, the resampled dataset will thus follow the Gaussian distribution, and the upper and lower ϵ with 95% confidence can thus be calculated.

3. RESULTS

3.1 Surface Meteorology

The wind speed data from the R/V Shikmona and three meteorology stations: Maabarot, Hadera, and Hamaapil stations, are compared (fig 3.1). The data from the ship, Maabarot station, and Hadera station have a temporal resolution of one minute, five minutes, and an hour, respectively. The Maabarot station is on land, and the Hadera station is about 1 km offshore on the pier of the power station and about 14 km away from the Maabarot station.

As can be seen from figure 3.1 (a), the wind speed data share a similar trend but the wind speed data from the Maabarot station had lesser magnitude and also presented a later response. The difference in magnitude and the time lag could be due to the difference in locations and the fact that Maabarot station is on the land. However, the wind data from the ship could be also affected by the free drifting of the ship. Therefore, to better calculate the response of the surface layer to wind forcing, the wind data from the Hadera station was used in this study.

The air temperature data were also compared, and as can be seen, the temperature data from the Maabarot station has a distinct difference daily variance likely due to the lower heat capacity of land compared to that of the sea. A similar trend can also be found in the relative humidity, where a distinct daily variance can be found at the Maabarot station, which could also be caused by the land-sea difference. The observed solar radiation from the R/V Shikmona and a land base station at Hamaapil were compared with the data from ECMWF ERA-5. As we can see, all data from different

data source share a comparable magnitude, and they all follow a similar trend with some minor difference. To obtain better observed results, we decided to choose wind speed data from Hadera station, and air temperature, pressure, relative humidity and net solar radiation data from R/V Shikmona.

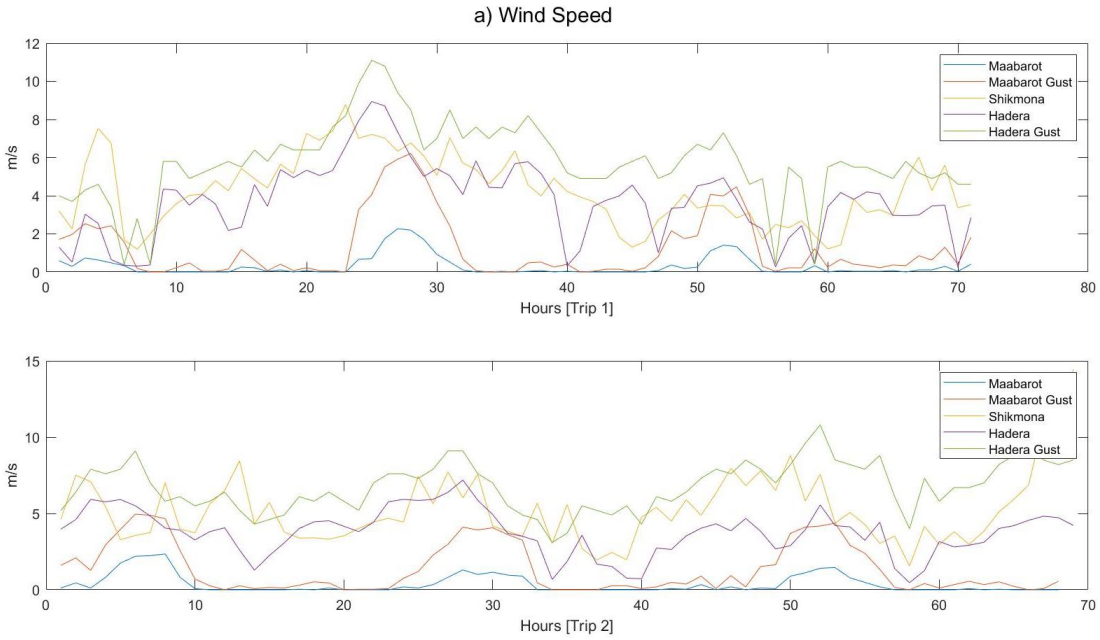

b) Air Temperature

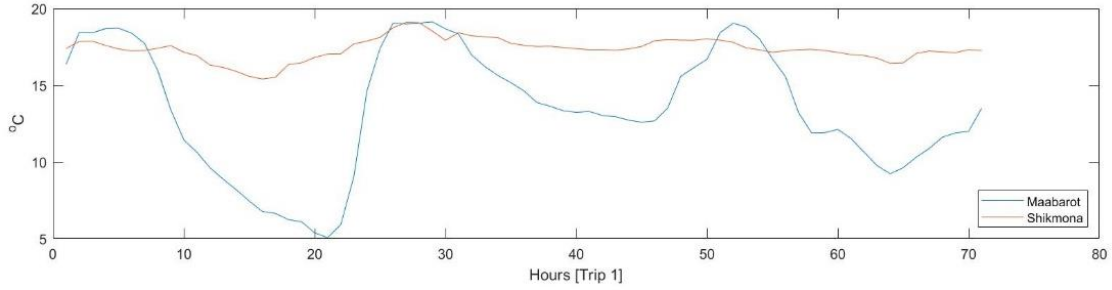

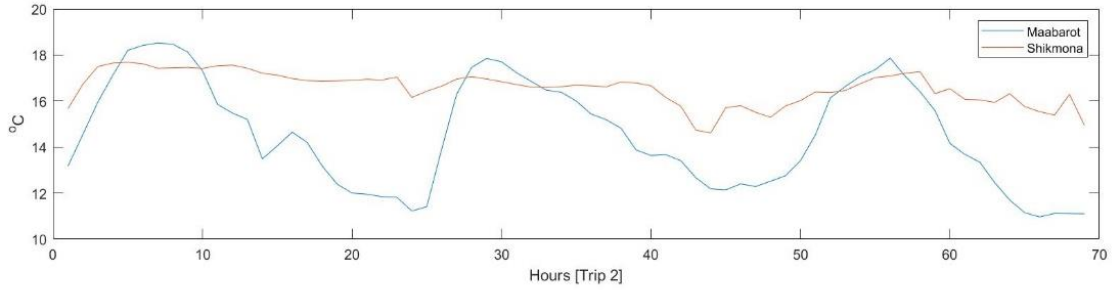

c) Pressure

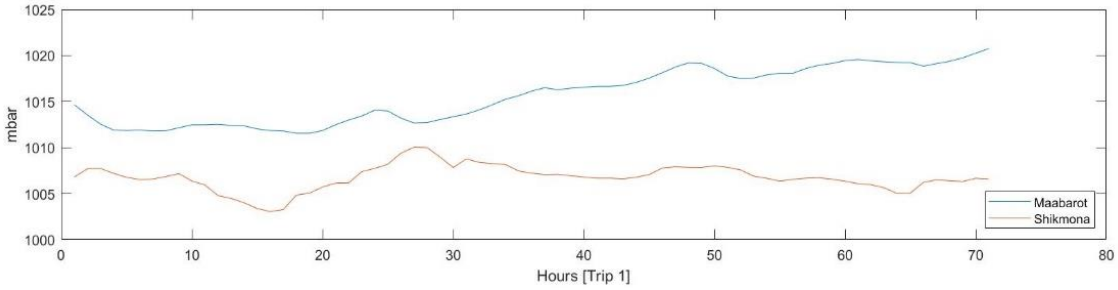

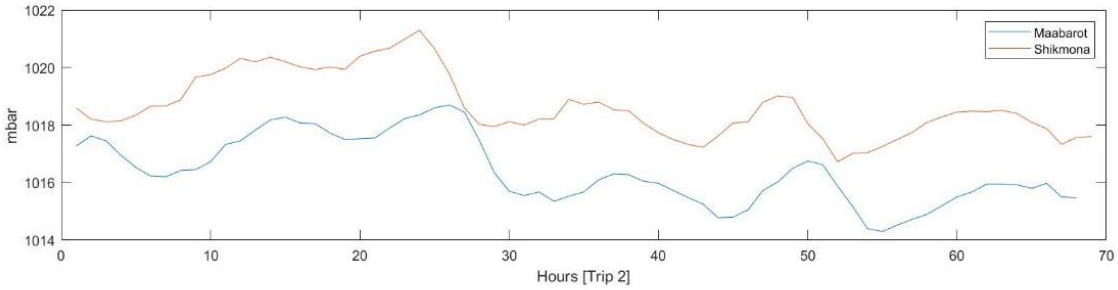

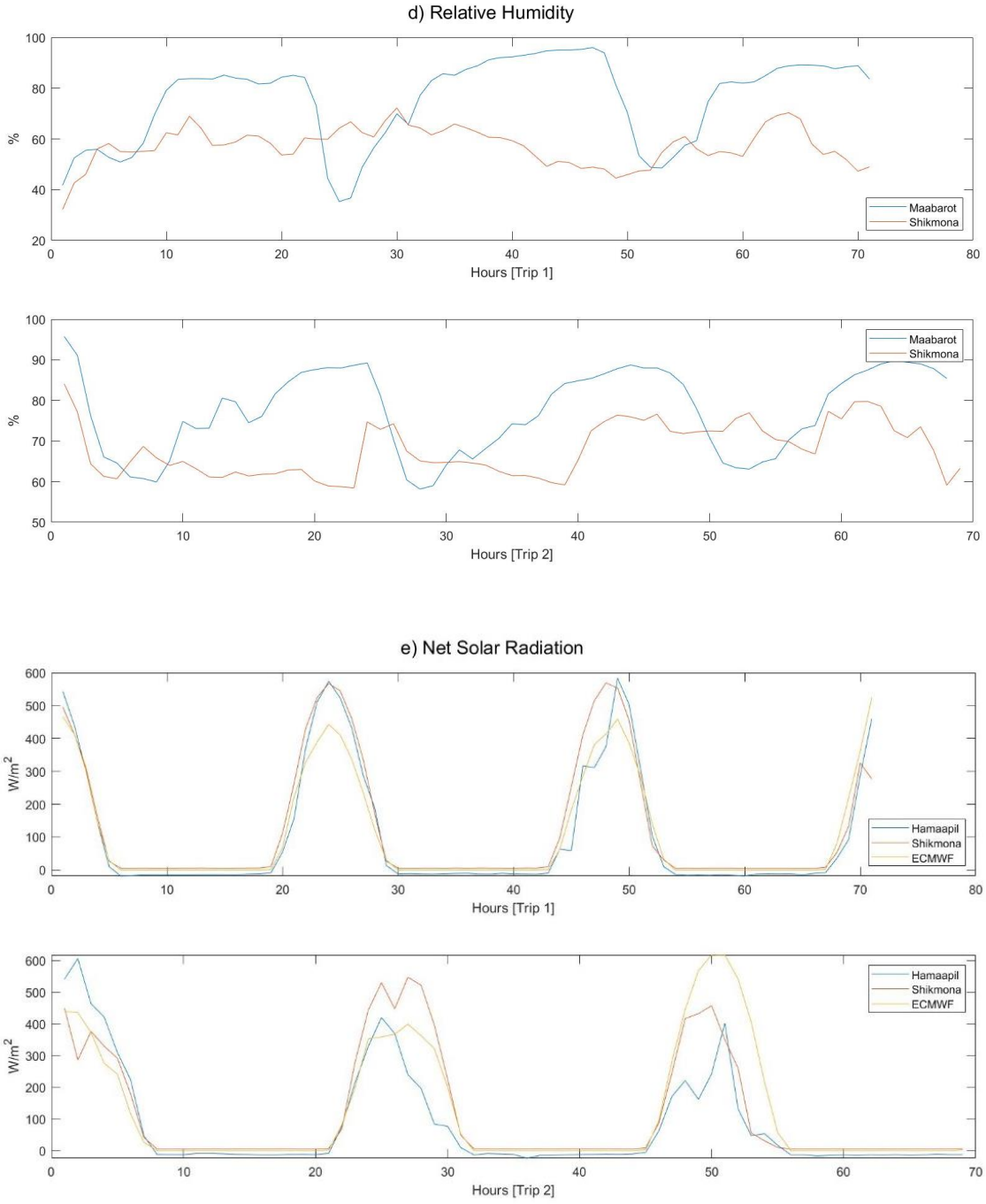

Figure 3.1 a) Wind speed data in m/s from Maabarot station, Hadera station and the Shikmona cruise, b) air temperature change figure title to Air Temperature , c) barometric pressure (change figure title accordingly), d) relative humidity from Maabarot station and R/V Shikmona, and e) net solar

radiation from ECMWF, R/V Shikmona and Hamaapil station. In all five subplots, the x-axis represents the hours since the beginning of the trip.

3.2 Surface Heat Fluxes

The observed and reanalysis wind stress data were calculated from the wind speed data of the Hadera station and the ECMWF ERA-5 with the following equation:

$$\tau = \rho_a C_d {u_{10}}^2 \quad (11)$$

where τ is the wind stress in N/m^2, C_d is the drag coefficient, and u_{10} is the wind speed at 10 meters height. As can be seen from the results (fig 3.2), in trip 1, the wind stress was less than 0.05 N/m^2 during most of the time, and only at noon of Jan 7, the wind stress showed a peak with a value of 0.12 N/m^2; in trip 2, the wind stress shows peaks in the evening of Jan 18 by 0.09 N/m^2, the morning of Jan 19 and 20 with values of 0.05 and 0.08 in N/m^2 respectively. The cubic of friction velocity is calculated from the wind stress and sea water density, and thus present the same trend in variation.

The observed sensible and latent heat fluxes were calculated from the observed surface meteorological data using the MATLAB air-sea toolbox (Fairall et al. 1996). The latent heat flux and the net solar radiation demonstrated similar trends in both the observed and reanalysis data, however the reanalysis sensible heat flux and long wave heat flux showed a clear daily variation, which was not found in the observed data.

For the heat budget in this region, the net heat flux, which were usually referred to as J_q^0, is about 500 W/m^2 in the daytime and -500 W/m^{-2} in the night. The net buoyancy flux, J_b^0, was estimated from the net surface heat flux (Anis et al., 2006) with values ranged between -10^{-7} to 10^{-7} m^2/s^3, due to the heat loss or gain. During daytime, the incoming radiation increased the stratification of the surface layer, and the buoyancy

flux was positive, but during night, the surface cooling increased near-surface mixing, and the buoyancy flux was thus negative. As a result, the M-O length, which is calculated from the ratio between J_b^0 and κu_*^3 (see Methods) will be negative during the night. The physical interpretation of M-O length is that the water column will be more influenced by wind stress above the M-O length, and more influenced by buoyancy flux beneath the M-O length. Therefore, a positive M-O length has no physical interpretation since it is above the sea surface.

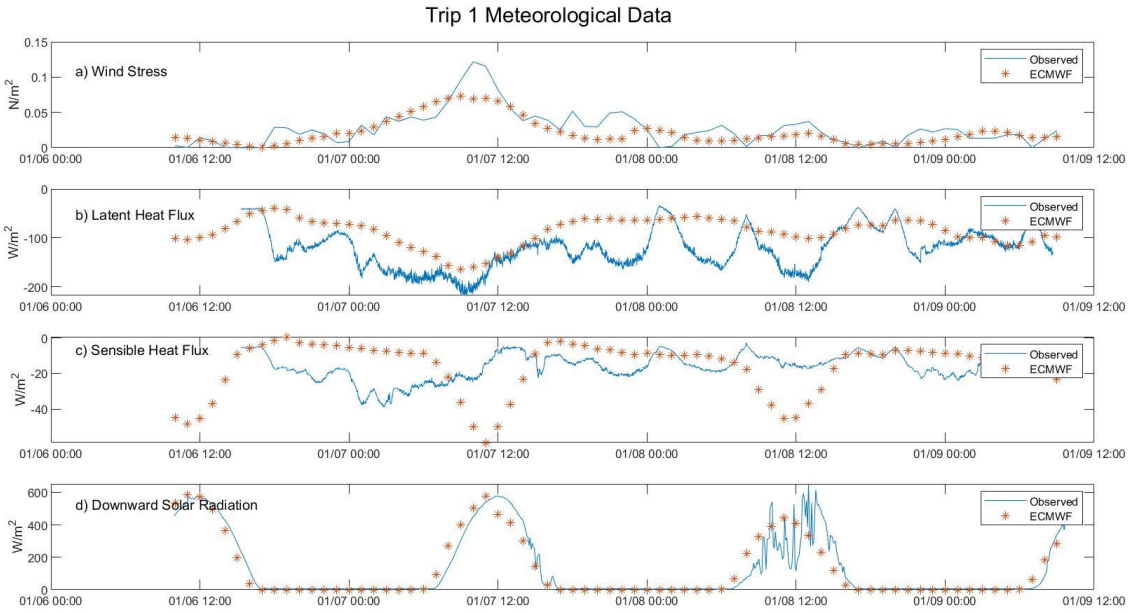

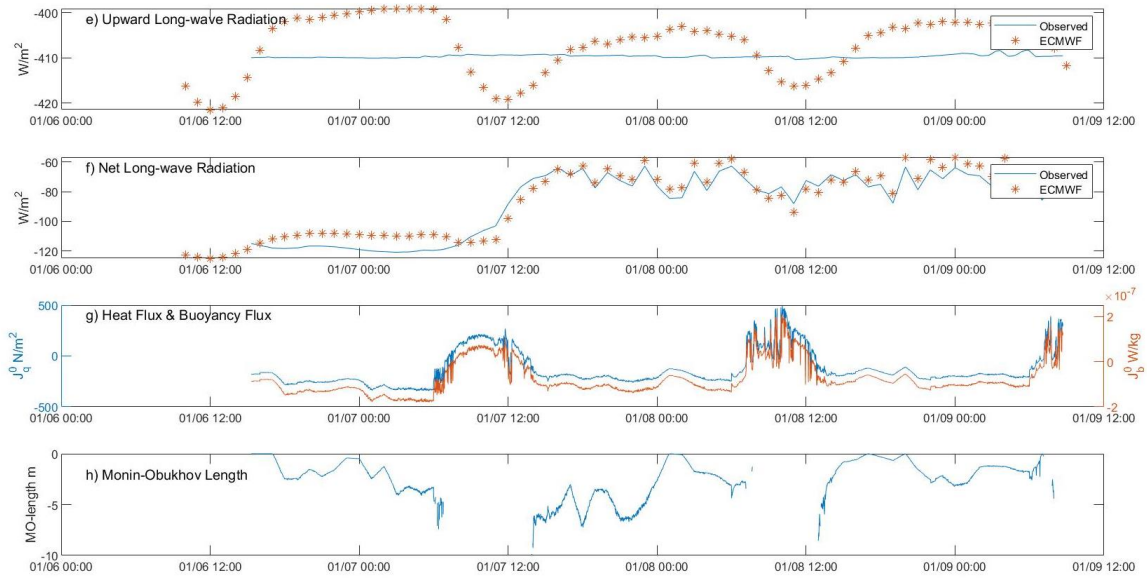

Figure 3.2 Surface meteorological data from trip 1, a) wind stress, b) latent heat flux, c) sensible heat flux, d) downward short-wave radiation, e) upward long wave radiation, f) net long wave radiation, g) net surface heat flux & surface buoyance flux, h) and M-O length.

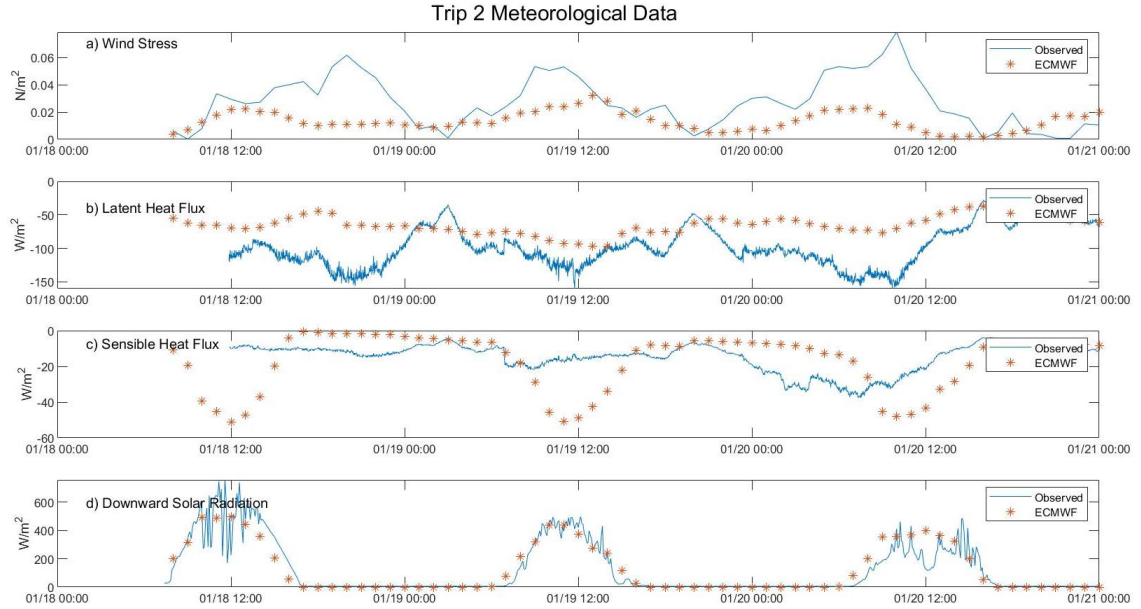

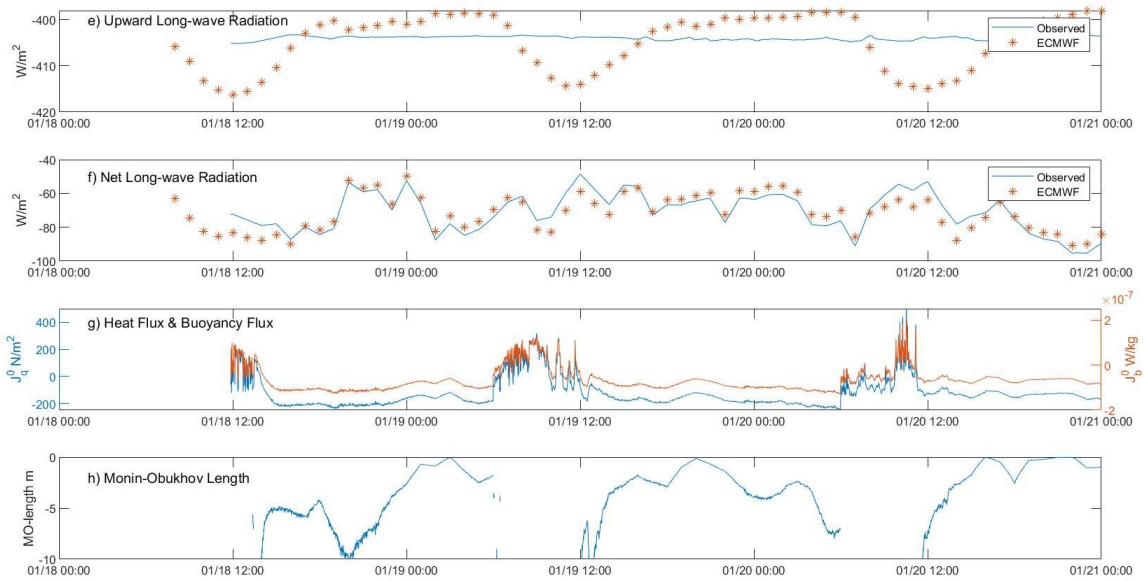

Figure 3.3 Surface meteorological data from trip 2, a) wind stress, b) latent heat flux, c) sensible heat flux, d) downward short-wave radiation, e) upward long wave radiation, f) net long wave radiation, g) net surface heat flux & surface buoyancy flux, h) and M-O length. For wind stress, latent heat flux, sensible heat flux, short wave radiation, upward long wave radiation, net long wave radiation, both the reanalysis results from ECMWF and the observed results are plotted for comparison.

3.3 Hydrographic data

For trip 1, all the samples were taken in a small region with depths ranging from 200-300 meters. Trip 2 was sampled across the shelf back and forth with depth ranging from less than 100 meters to 300 meters.

Through the whole water column, the temperature was between 16-20℃ and the salinity was ~39 PSU. As can be seen from figure 3.3, the whole water column can be separated into two sections: the upper well-mixed water (0-250m), and the bottom shelf water (250m-bottom). From the profiles of trip 1, we can observe that the boundary between them was around the depth of 220 meters, which may indicate that strong wind

events in winter may be able to mix the water down to that depth. The temperature of the well mixed water was about 20℃, and the bottom water about 16℃. The salinity of the well mixed water was about 39.6ppt, and the bottom water about 38.8ppt. Thus, the bottom water was colder but less saline than the well-mixed water column (fig 3.4). Separate figs for trip 1 and 2 and renumber as needed.

From the results of trip 2 (fig 3.4), we can find that for shallower profiles (less than 100-meter depth) the water column was well mixed from the top to the bottom, and for deeper profiles, it presents a similar pattern as the profiles in trip 1, characterized by a deep mixing layer about 220 meters and the colder and fresher bottom water beneath it.

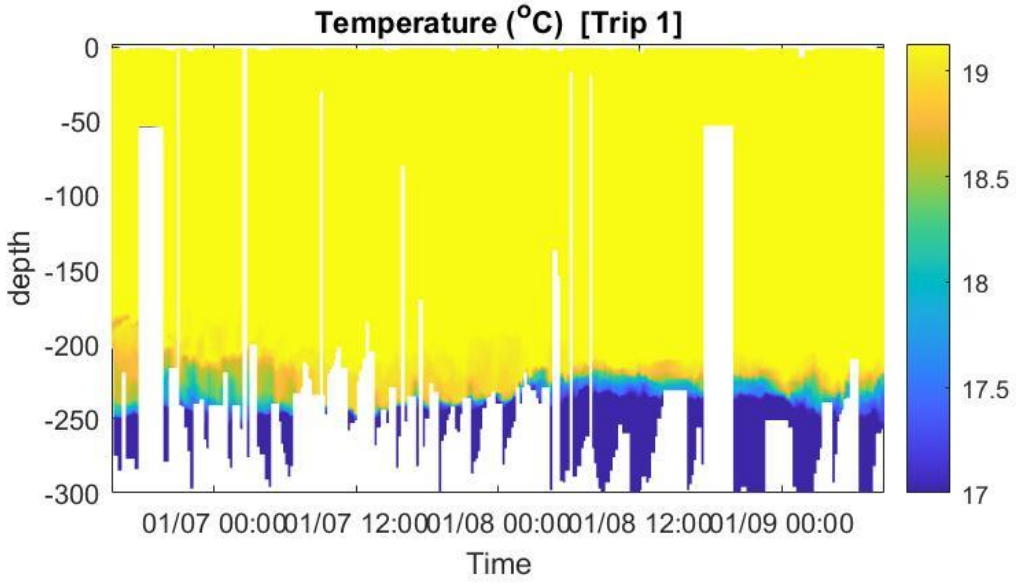
Temperature (°C) [Trip 1]
0
-50
-100
-150
-200
-250
-300
depth
01/07 00:00
01/07 12:00
01/08 00:00
01/08 12:00
01/09 00:00
Time
19
18.5
18
17.5
17

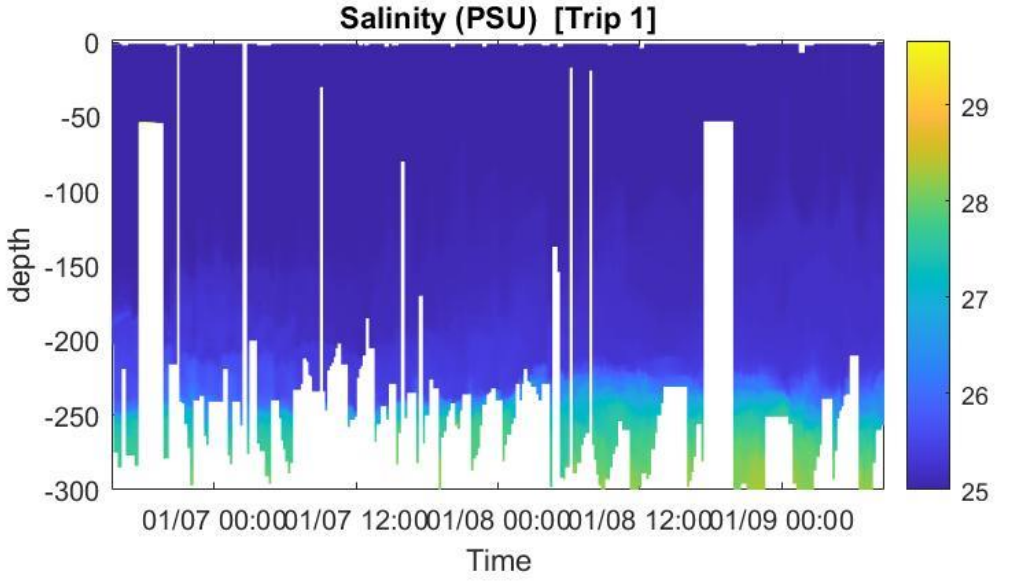
Salinity (PSU) [Trip 1]
0
-50
-100
-150
-200
-250
-300
depth
01/07 00:00
01/07 12:00
01/08 00:00
01/08 12:00
01/09 00:00
Time
29
28
27
26
25

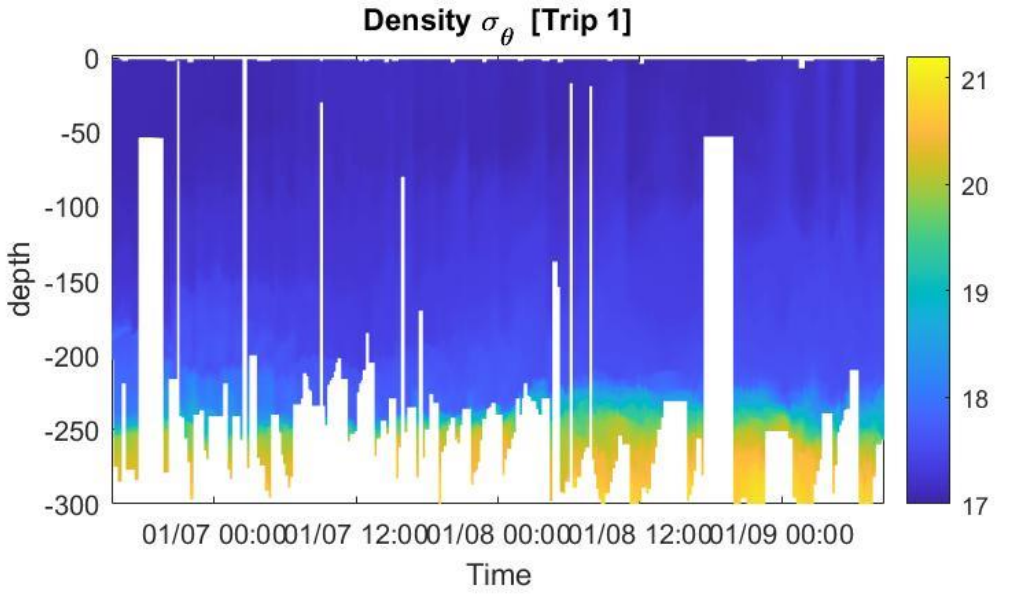
Density σ_θ [Trip 1]
depth
0
-50
-100
-150
-200
-250
-300
01/07 00:00
01/07 12:00
01/08 00:00
01/08 12:00
01/09 00:00
Time
21
20
19
18
17

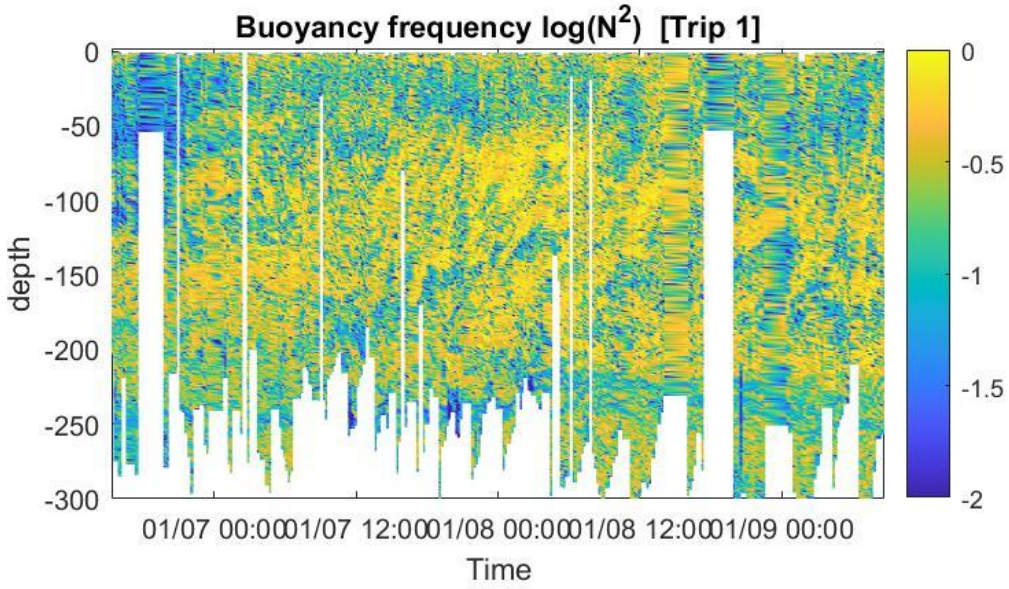
Buoyancy frequency log(N^2) [Trip 1]
depth
0
-50
-100
-150
-200
-250
-300
01/07 00:00
01/07 12:00
01/08 00:00
01/08 12:00
01/09 00:00
Time
0
-0.5
-1
-1.5
-2

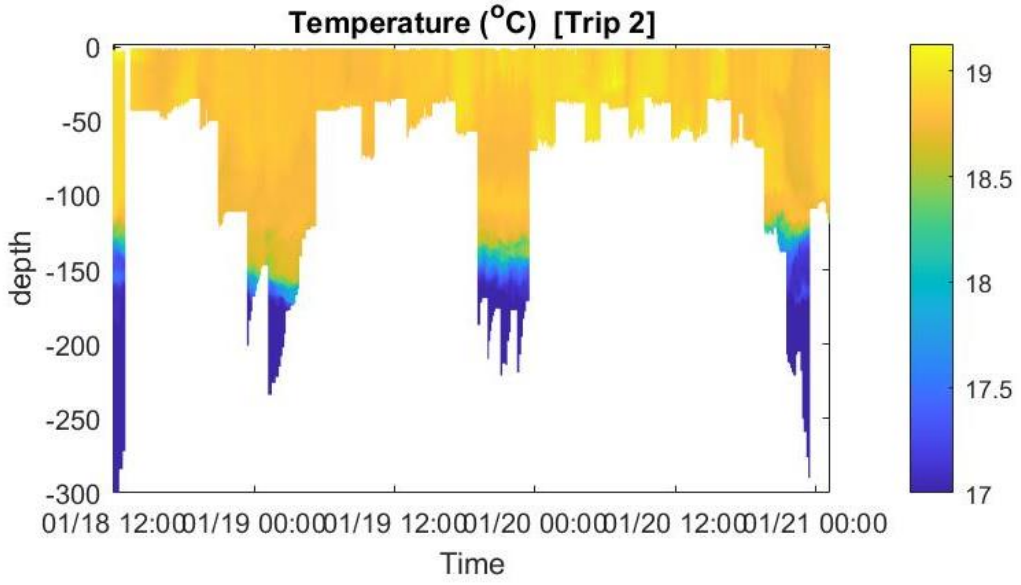
Temperature (°C) [Trip 2]
0
-50
-100
-150
-200
-250
-300
depth
01/18 12:00
01/19 00:00
01/19 12:00
01/20 00:00
01/20 12:00
01/21 00:00
Time
19
18.5
18
17.5
17

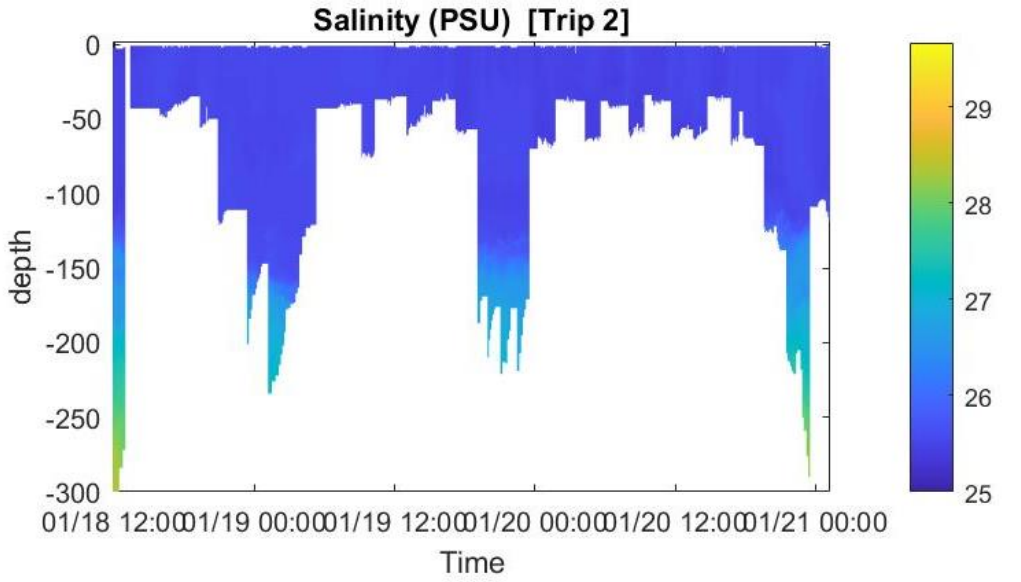
Salinity (PSU) [Trip 2]
0
-50
-100
-150
-200
-250
-300
depth
01/18 12:00
01/19 00:00
01/19 12:00
01/20 00:00
01/20 12:00
01/21 00:00
Time
29
28
27
26
25

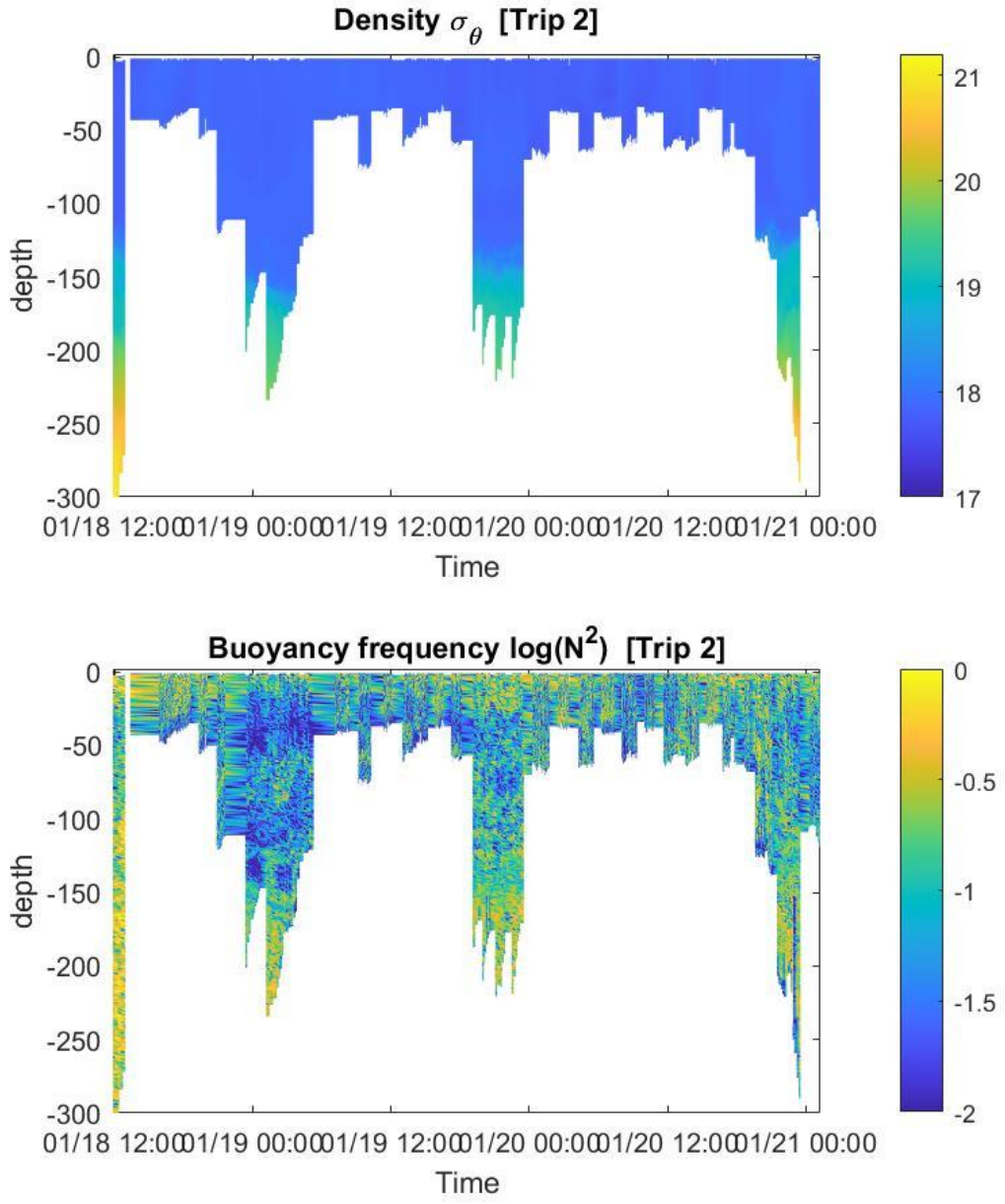

Figure 3.4 Hydrographic data from trip 1 and trip 2, including temperature, salinity, density, and buoyancy frequency; the x-axis represents the sampling time, and the y-axis shows the depth in meters.

3.4 TKE Dissipation Rates

3.4.1 Microstructure Shear Spectra

The shear data were collected from two shear sensors, oriented perpendicular to each other, and mounted at the nose of the microstructure profiler (see methods). The shear data was edited to remove signals coherent with spikes in the acceleration signal. Then the shear signals were binned into intervals with 3072 data points each., Since the sampling frequency of the sensors was 1024 Hz, the 3072 data points represent 3 seconds and about 2-meter bins in the vertical.

The shear signals within each bin was converted into power spectrum density using the Welch method (Welch 1967), and then fitted to the Nasmyth empirical spectra (Nasmyth, 1970) using three different methods: MSS, MLE, and Lueck (Lueck, 2013; Stips et al., 2000; Ruddick et al., 2000). The following figures are examples from 5 different depth intervals (36.74m - 38.72m, 78.35m - 80.48m, 120.56m - 122.68m, 163.15m - 165.30m, 206.21m - 208.38m) in profile 120, trip 1 (fig 3.6). The observed spectrum was plotted in blue together with the three fitted spectra.

The Nasmyth spectrum was fitted from an upper cutoff wavenumber, which was set to 2 cycle per meter (cpm) to the Kolmogorov wavenumber around 100 cpm. In general, the power spectrum density increased slightly from ~2 cpm to ~10 cpm, while decreasing quickly from ~10 cpm to ~100 cpm. At frequencies higher than the Kolmogorov wavenumber spectra were dominated by high frequency instrument noise. The dissipation rates calculated through the fitting with the different methods are listed on each of the plots.

Trip 1, Profile 120, Depth: 36.7478(m) to 38.7254(m)

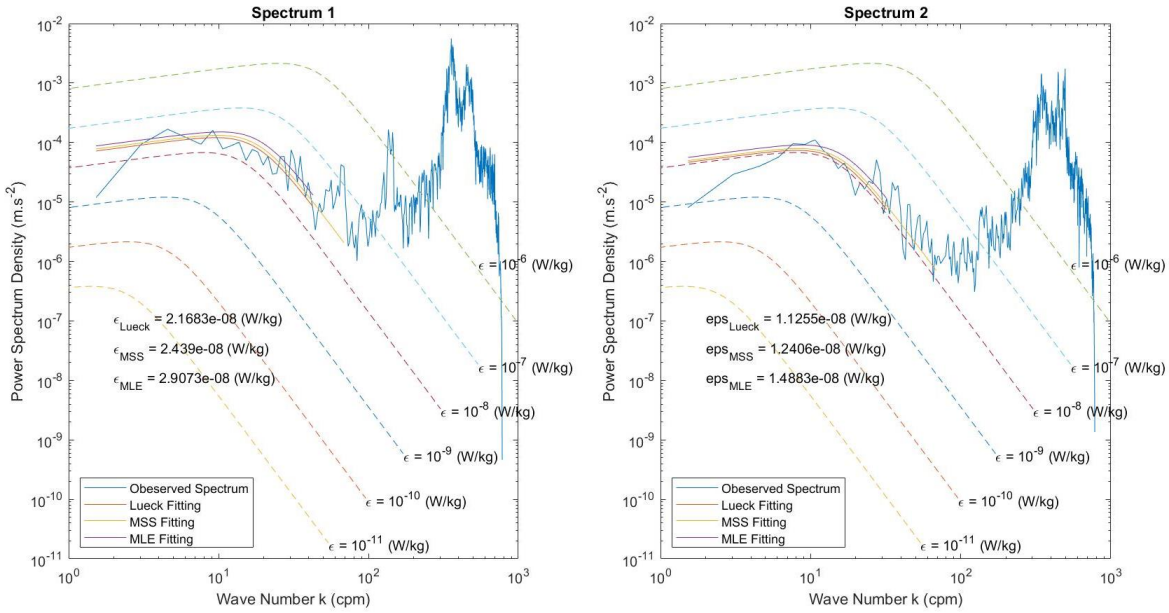

Trip 1, Profile 120, Depth: 78.3528(m) to 80.4827(m)

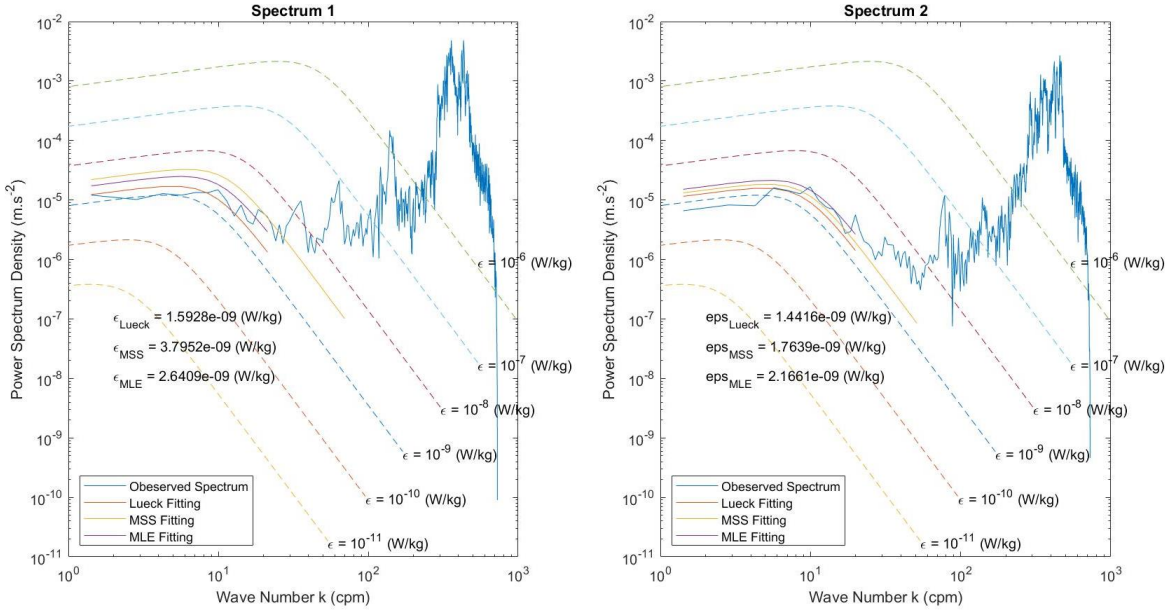

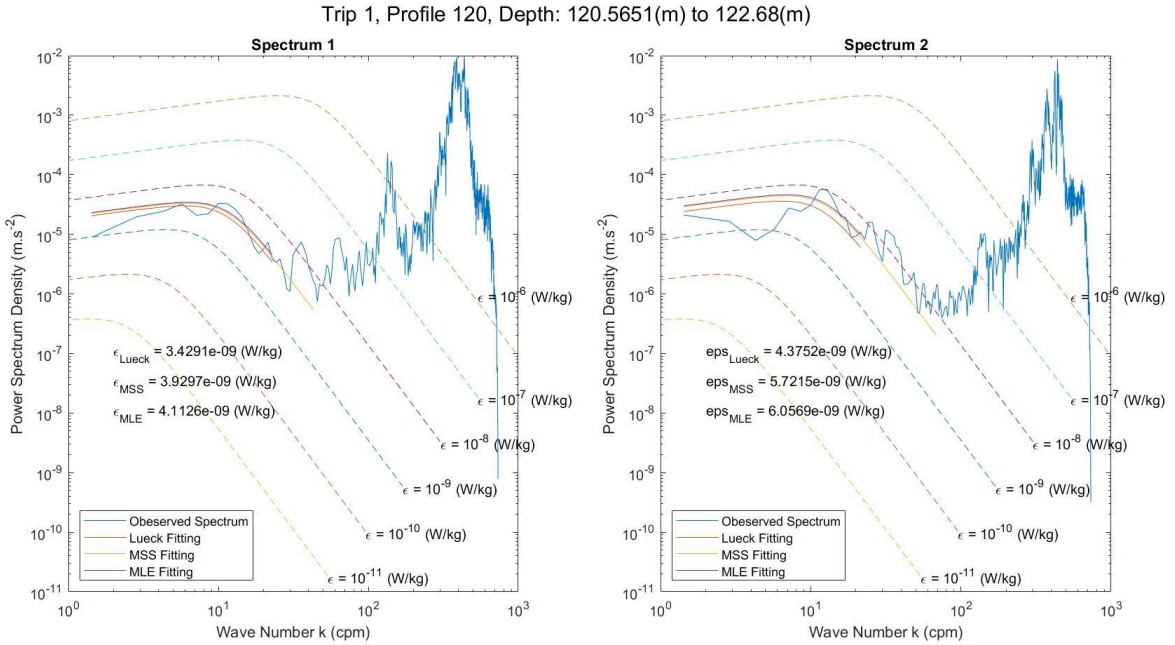
Trip 1, Profile 120, Depth: 120.5651(m) to 122.68(m)
Spectrum 1
Spectrum 2
Power Spectrum Density (m.s-2)
Wave Number k (cpm)
ϵLueck = 3.4291e-09 (W/kg)
ϵMSS = 3.9297e-09 (W/kg)
ϵMLE = 4.1126e-09 (W/kg)
epsLueck = 4.3752e-09 (W/kg)
epsMSS = 5.7215e-09 (W/kg)
epsMLE = 6.0569e-09 (W/kg)
ϵ = 10-6 (W/kg)
ϵ = 10-7 (W/kg)
ϵ = 10-8 (W/kg)
ϵ = 10-9 (W/kg)
ϵ = 10-10 (W/kg)
ϵ = 10-11 (W/kg)
Obeserved Spectrum
Lueck Fitting
MSS Fitting
MLE Fitting

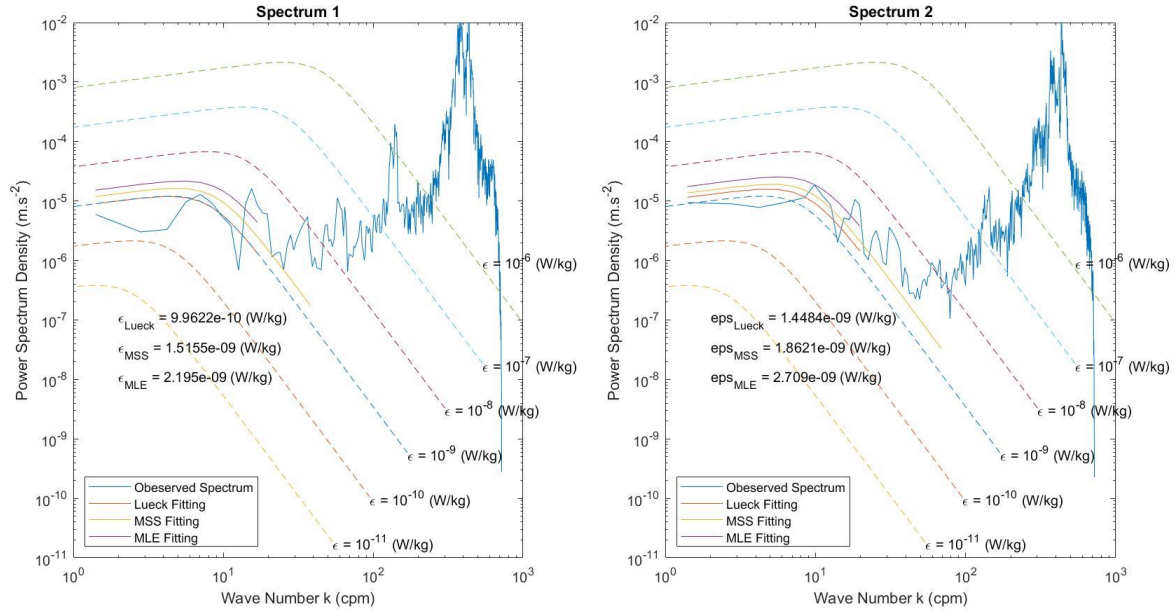
Trip 1, Profile 120, Depth: 163.1482(m) to 165.2956(m)
Spectrum 1
Spectrum 2
Power Spectrum Density (m.s-2)
Wave Number k (cpm)
ϵLueck = 9.9622e-10 (W/kg)
ϵMSS = 1.5155e-09 (W/kg)
ϵMLE = 2.195e-09 (W/kg)
epsLueck = 1.4484e-09 (W/kg)
epsMSS = 1.8621e-09 (W/kg)
epsMLE = 2.709e-09 (W/kg)
ϵ = 10-6 (W/kg)
ϵ = 10-7 (W/kg)
ϵ = 10-8 (W/kg)
ϵ = 10-9 (W/kg)
ϵ = 10-10 (W/kg)
ϵ = 10-11 (W/kg)
Obeserved Spectrum
Lueck Fitting
MSS Fitting
MLE Fitting

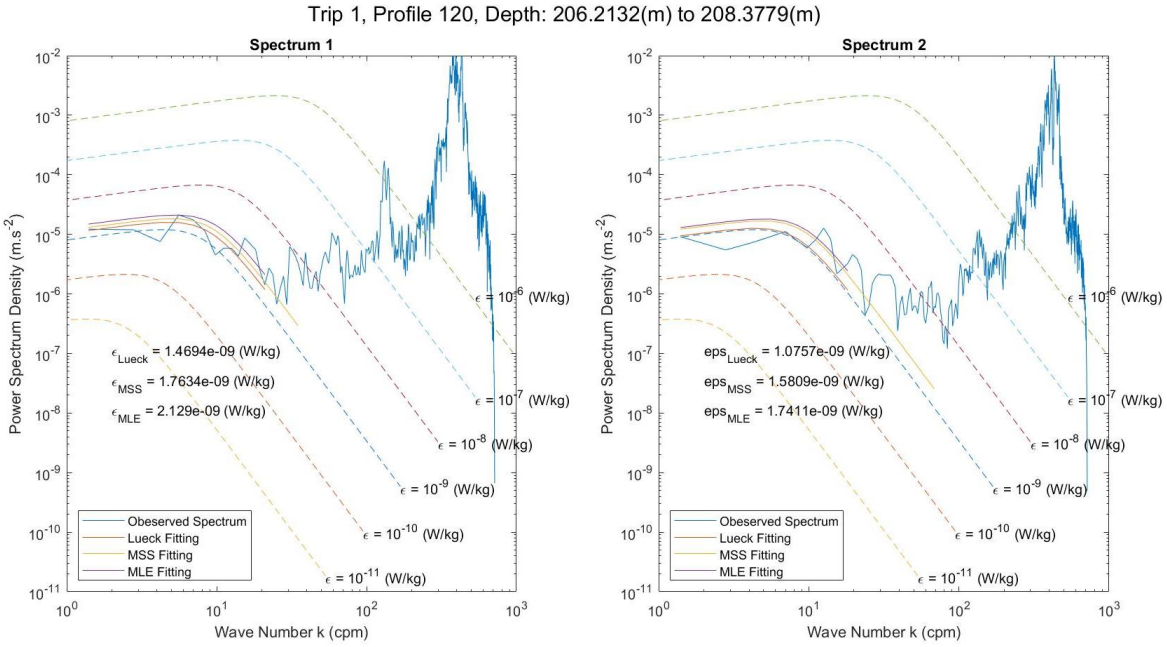

Figure 3.5 Observed shear spectra and fitted Nasmyth empirical spectra using 3 different methods at selected depth intervals in profile 120, trip 1.

3.4.2 TKE Dissipation Rate Profiles

The TKE dissipation rates from profile 140 in trip 1 are plotted (fig 3.6) and showed as an example. The total depth of this profile is 267 meters with 395434 data points, and the profile was binned into 128 segments, with 3072 data points (~ 2 meters) in each. The potential density of this profile is also plotted for reference.

As can be seen from the figure of trip 1, from the surface to a depth of ~75 meters, the water column was well mixed with the same potential density of about 1028.16 kg/m^3, and a TKE dissipation rate, ϵ, of ~10^{-7} W/kg. Deeper, the potential density increases slightly, and the dissipation rates drop quickly to about 10^{-9} W/kg. Between

200 to 240 meters, the potential density stays roughly the same at 1028.45 kg/m^3, and the dissipation rate peaks to 10^{-7} W/kg at about 220 meters.

When the potential density stays at the same value within an interval, we may infer that the water column is likely well-mixed in that depth range, and the dissipation rates will be relatively large. If the potential density increases with depth, we may infer that the water column is stratified in that depth range, and the dissipation rate will likely decrease. The same behavior can also be found in other profiles.

By comparing profiles 80, 140 from trip 1, we can find that in this region, the surface mixed layer was about 50 – 100 meters deep, characterized by a roughly constant potential density and relatively large dissipation rates of about 10^{-7} W/kg. Potential density increased beneath the surface mixed layer to about 200 meters, while the dissipation rate remained at about 10^{-9} W/kg in this depth range. Beneath that, the shelf, near-bottom, water with a stable potential density, exhibited higher dissipation rates peaking at about 10^{-7} W/kg, suggesting elevated mixing events to occur in the bottom boundary layer.

All the profiles in trip 2 can be classified into 3 categories by the total depth: profiles less than 100 meters, profiles less than 250 meters, and profiles more than 250 meters.

For profiles less than 100 meters, the whole water column was mostly dominated by well-mixed surface water, with a stable potential density and dissipation rates above 10^{-8} W/kg. Near the bottom, the potential density increased and a following decrease in dissipation rates was observed at the same depth.

For profiles deeper than 100 meters but shallower than 250 meters, the upper layer (shallower than 70 meters here) shared a similar structure to profiles that were less than 100 meters in depth. Beneath that, the potential density decreased and dissipation rates dropped below 10^{-8} W/kg.

For profiles more than 250 meters deep, the water columns shared similar properties as profiles less than 250 meters in depth, but near the bottom, the potential density was stable (1029.1 kg/m^3 in this case), and dissipation rates peaked in the same depth range.

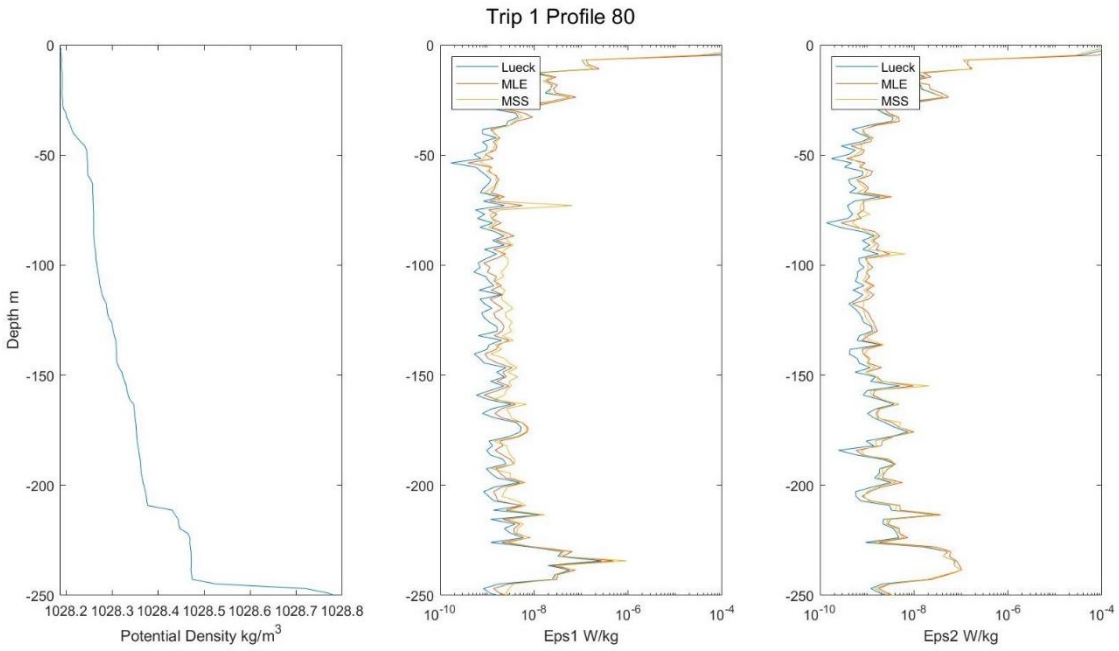

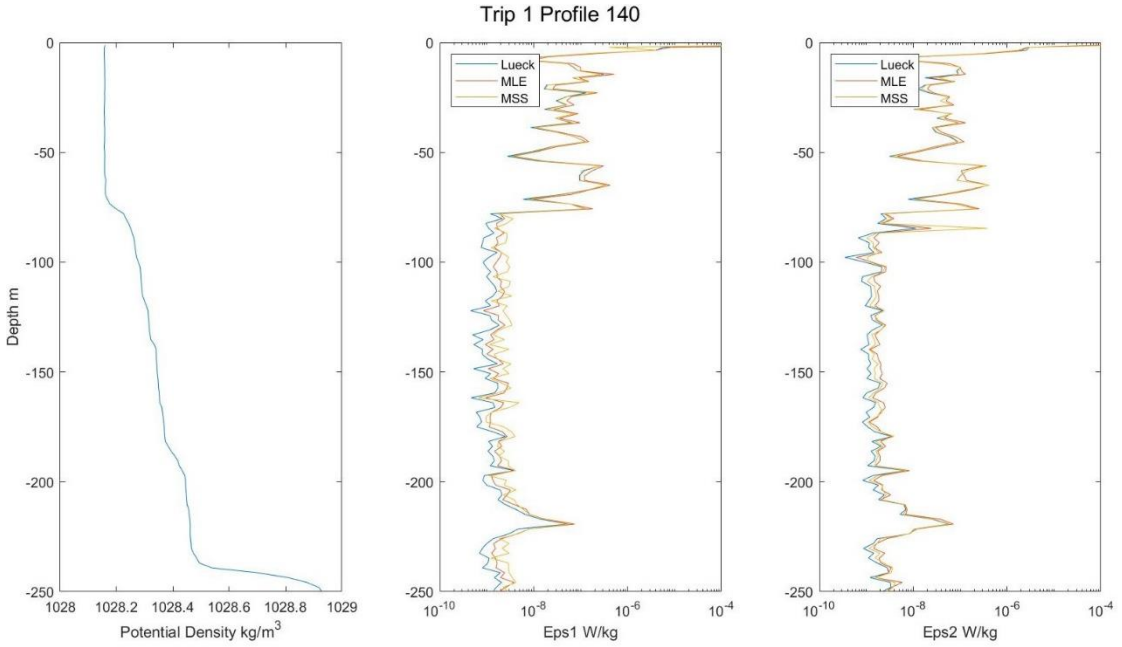
Trip 1 Profile 140
Depth m
Potential Density kg/m3
Eps1 W/kg
Eps2 W/kg
Lueck
MLE
MSS

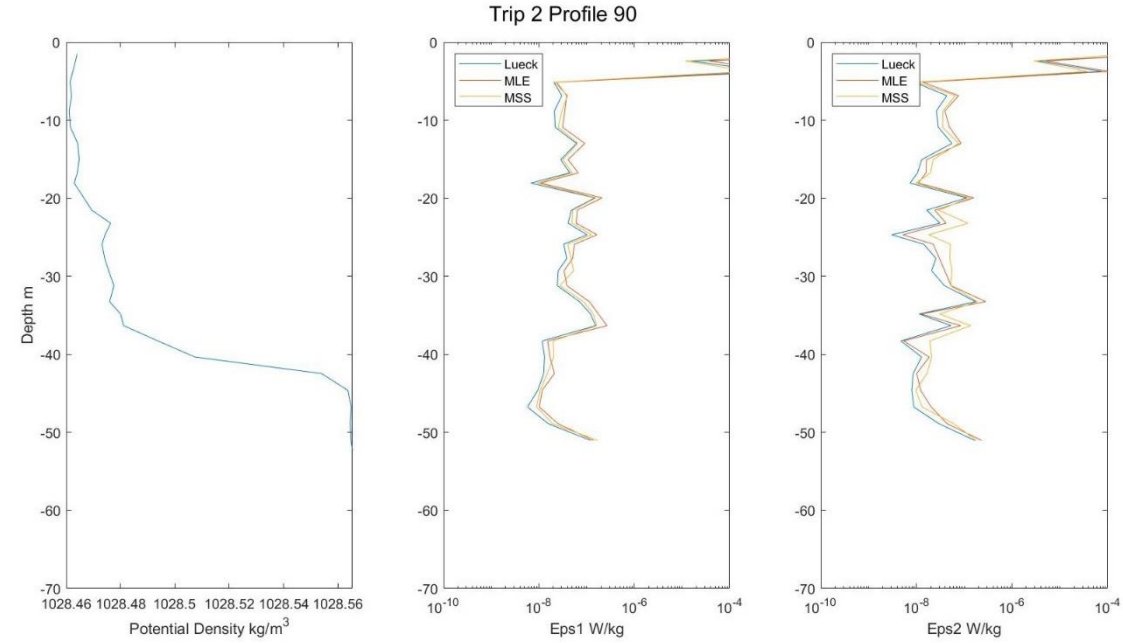
Trip 2 Profile 90
Depth m
Potential Density kg/m3
Eps1 W/kg
Eps2 W/kg
Lueck
MLE
MSS

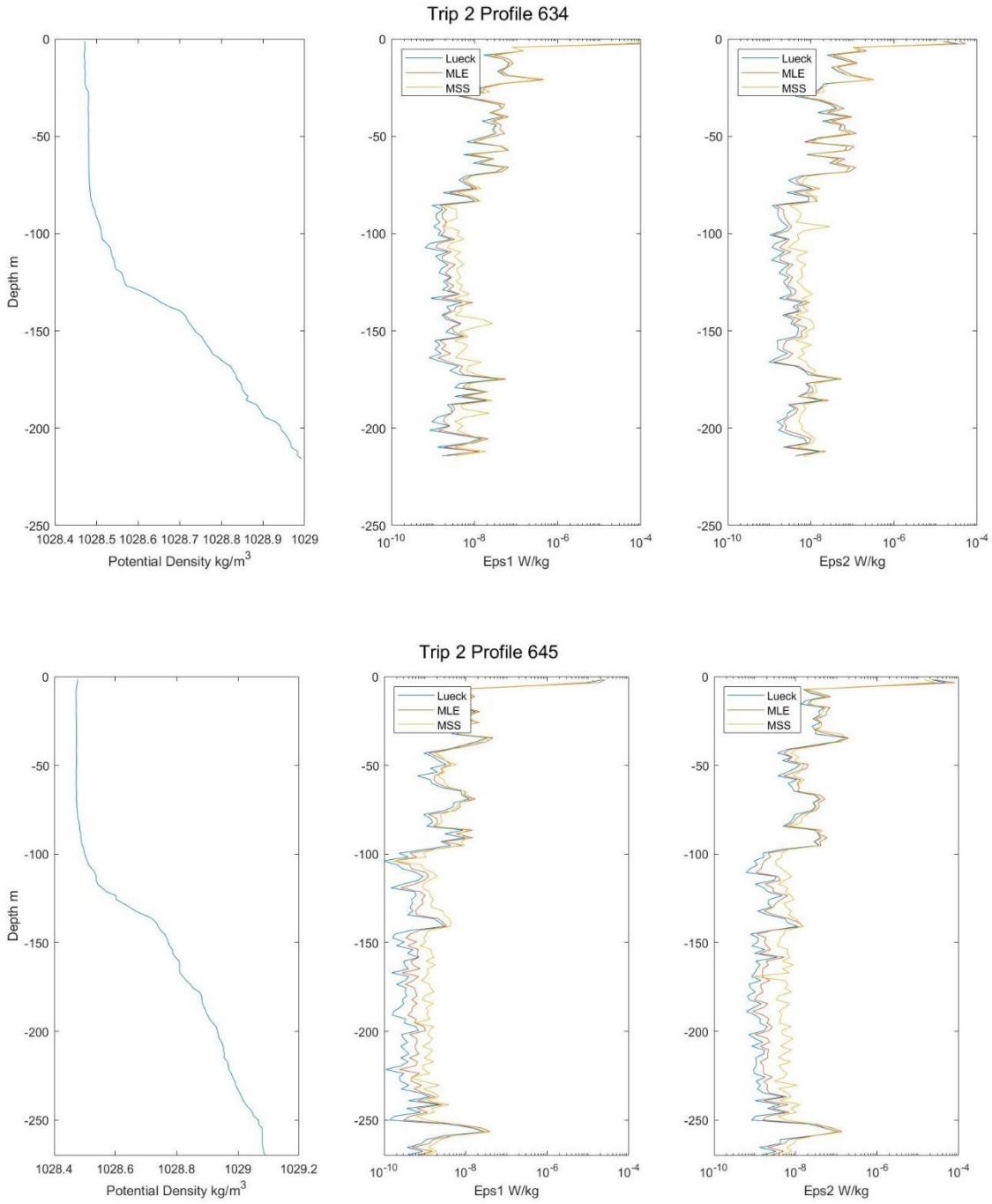

Figure 3.6 Profiles of potential density on leftmost (density) panel and TKE dissipation rates estimated from the two shear sensors from profiles 140 and 80, trip 1, and profiles 90, 634, 645, trip 2.

3.5 Scaling of TKE Dissipation Rates

The increase of turbulent mixing in the surface layer is due to two main sources: surface cooling, and wind stress. The mixing due to surface cooling can be estimated through the buoyancy flux, ϵ_c,, while turbulent mixing due to wind stirring, ϵ_w, may be assessed from the following equation (e.g. Anis, 2006):

$$\epsilon_w = \frac{{u_*}^3}{\kappa z}, \epsilon_c \approx J_b^0$$

Here, u_* is the water-surface friction velocity, which can be calculated from wind stress and the density of seawater, κ is the Karman constant (~0.41), and z is the depth, which is in the denominator since the influence of wind is decreasing through depth.

During daytime, the incoming short-wave solar radiation is absorbed, heats the surface layer, increases stratification, and decreases turbulent mixing. Therefore, profiles from daytime are not discussed here. ϵ_w and ϵ_c share a similar magnitude and dimension as the dissipation rates, and as a result, these three parameters can be plotted on the same plot to determine which of the two forcings is more significant in driving mixing.

In the following figures, the dissipation rate profiles are compared to ϵ_w and ϵ_c, calculated from observed meteorological data (See Methods). The mixed layer depth was taken as the depth at which the maximum vertical density gradient was observed, and the depth was normalized by dividing with the mixed layer depth. The M-O lengths, the ratio between ${u_*}^3$ and κJ_b^0, were also plotted on each plot, which is the depth where $\epsilon_w = \epsilon_c$.

Trip: 1, Profile: 35, Time: Wed Jan 07 01:18:35 2009, Mixing Layer: 46 (m)

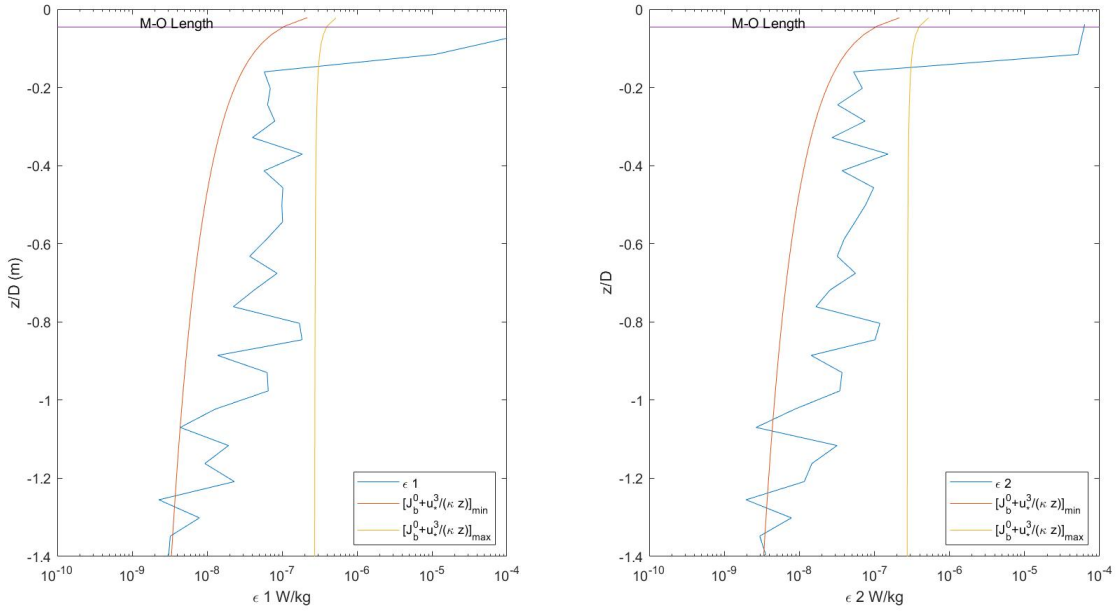

Trip: 1, Profile: 134, Time: Wed Jan 07 23:12:41 2009, Mixing Layer: 60 (m)

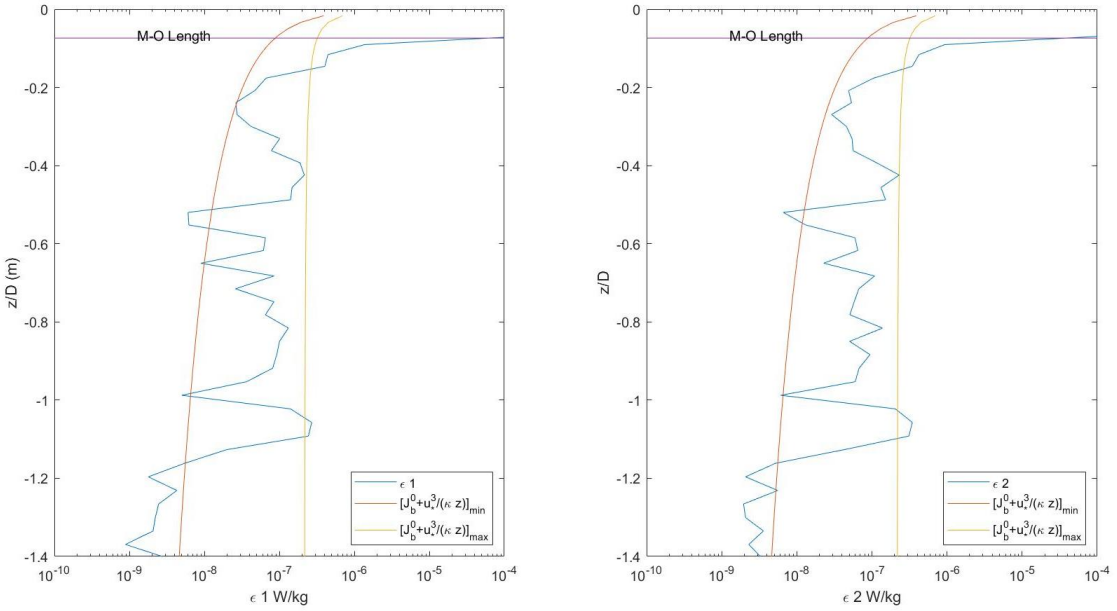

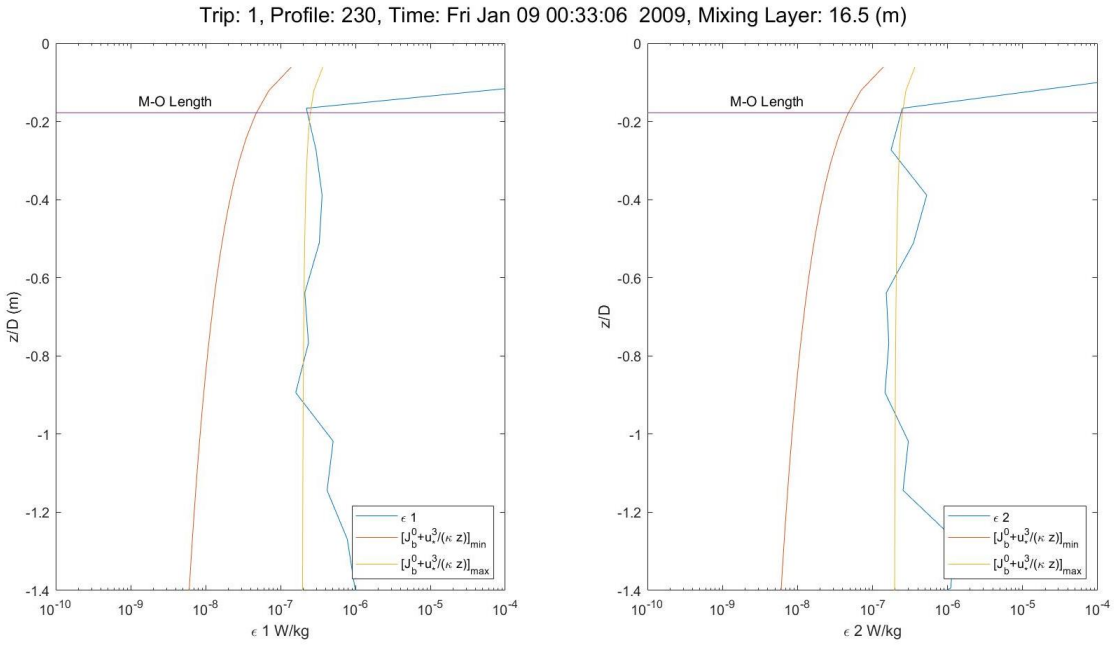

Figure 3.7 Scaling example results from profile 35, 134, and 230, trip 1, during the nights of Jan 6, 7, and 8.

The examples above are selected from three different nights in trip 1 and plotted against z/D, depth over mixing layer depth. The max and min value about averaged $[J_b^0+u_*^3/\kappa z]$ of each night from the bootstrap method with 95% confidence are also plotted. As can be seen from the results, the dissipation rates dropped dramatically from the surface to around the M-O depth, and roughly follow a value of ~10^{-7} W/kg beneath that. Also, from the result of wind stress and wind velocity, during trip 1, only in Jan 6th, did the wind speed reach 6.931 m/s with a wind stress about 0.073 N/m^2, and for the other profiles, the wind condition was clam with wind speed less than 5 m/s and the wind stress less than 0.035 N/m^2. Therefore, the dissipation rate is more correlated to the buoyancy flux, instead of the wind.

Trip: 2, Profile: 108, Time: Mon Jan 19 00:12:25 2009, Mixing Layer: 70 (m)

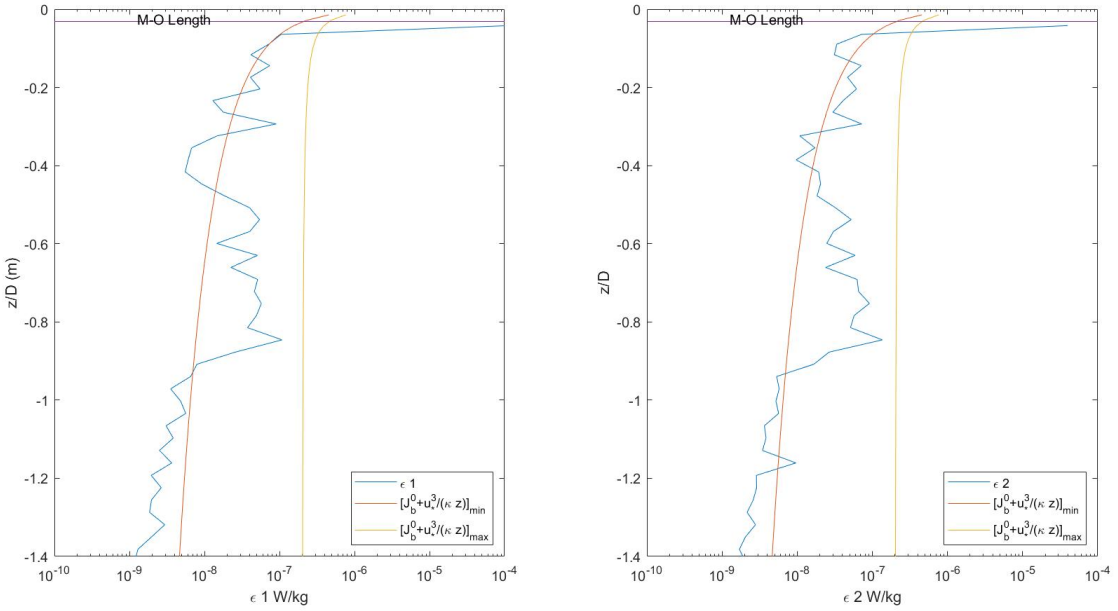

Trip: 2, Profile: 340, Time: Tue Jan 20 00:45:33 2009, Mixing Layer: 62.5 (m)

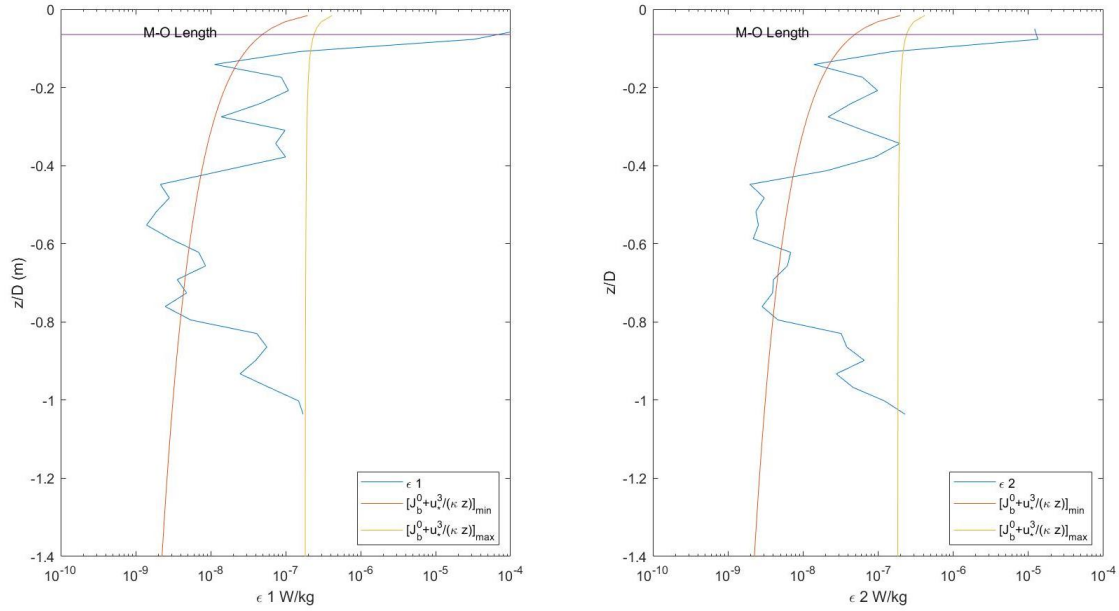

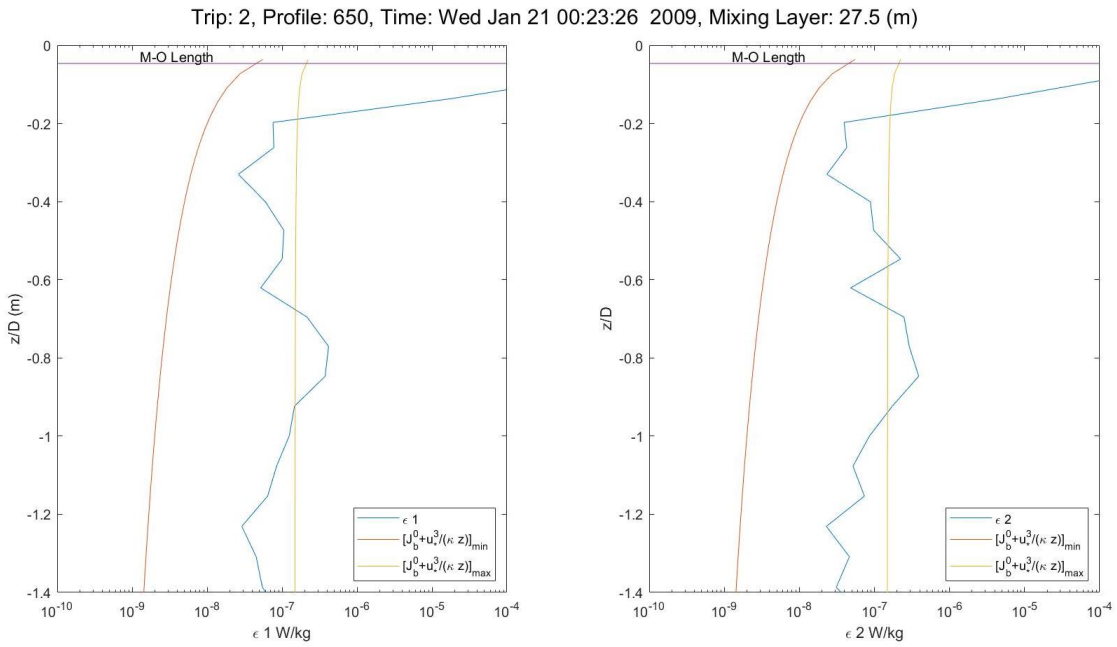

Figure 3.8 Scaling results for profiles 108, 340, and 650, trip 1, during the nights of Jan 18, 19, and 20.

However, for the profile 108, 340 in trip 2, during the night of Jan 18 and 19, with larger wind stress, the mixing layer depth is 70m, 62.5m respectively. The dissipation rate showed a decreasing trend with depth, which is similar to ϵ_w. In profile 650, during the night of Jan 20, the wind stress is less, and the mixing layer depth is 27.5m. The variation of dissipation rate with depth is of a minor magnitude (fig. 3.8).

4. DISCUSSION

4.1 Water Column Structure on the Israel Shelf in Winter

The basic structure of the water column was dominated by a downwelling system. The northward wind stress in the winter drove water ashore via the Ekman transport mechanism (Price et al. 1987), which piled up water along the shore, and created the downwelling system. The downwelling system was characterized by a deepened pycnocline, at about 100-300 meters. This feature was also found in previous studies (e.g. Fig 3 in Rosentraub et al., 2007, reproduced here in Fig 4.1) as well as in our study during the two trips (fig 4.2).

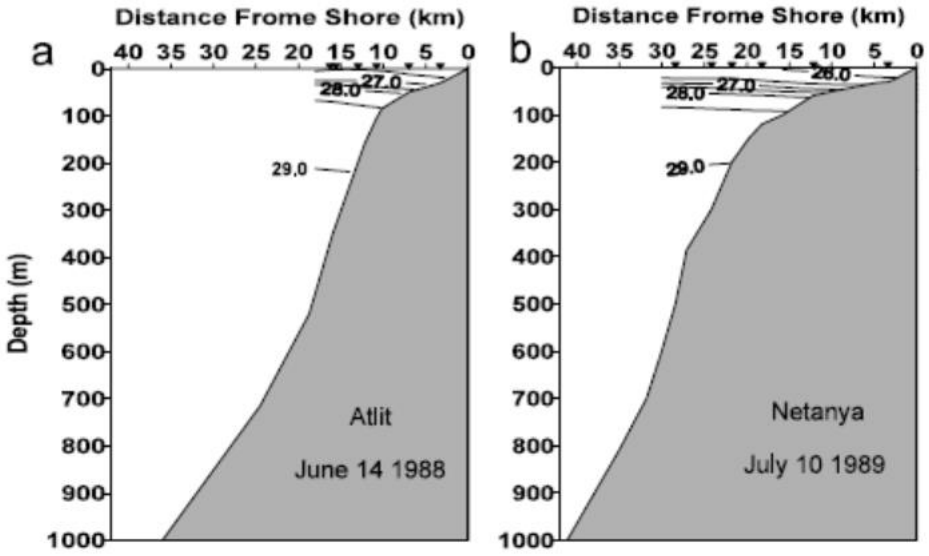

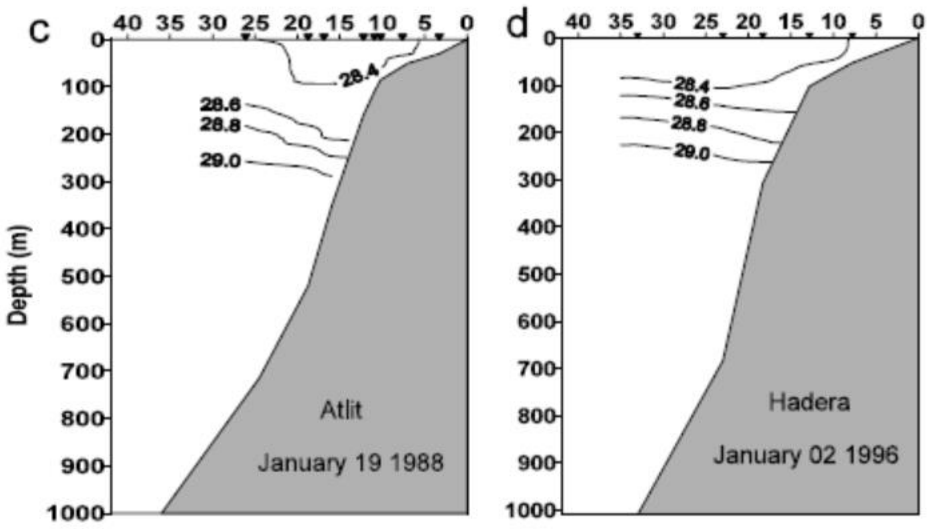

Figure 4.1 Cross shelf density profiles on the Israel shelf, at a) Atlit on June 14, 1988, b) Natanya on July 10, 1989, c) Atlit on Jan 19, 1988, and d) Hadera on Jan 2, 1996. (Rosentraub et al., 2007) a) and b) are from summer profiles and c) and d) are observed in winter.

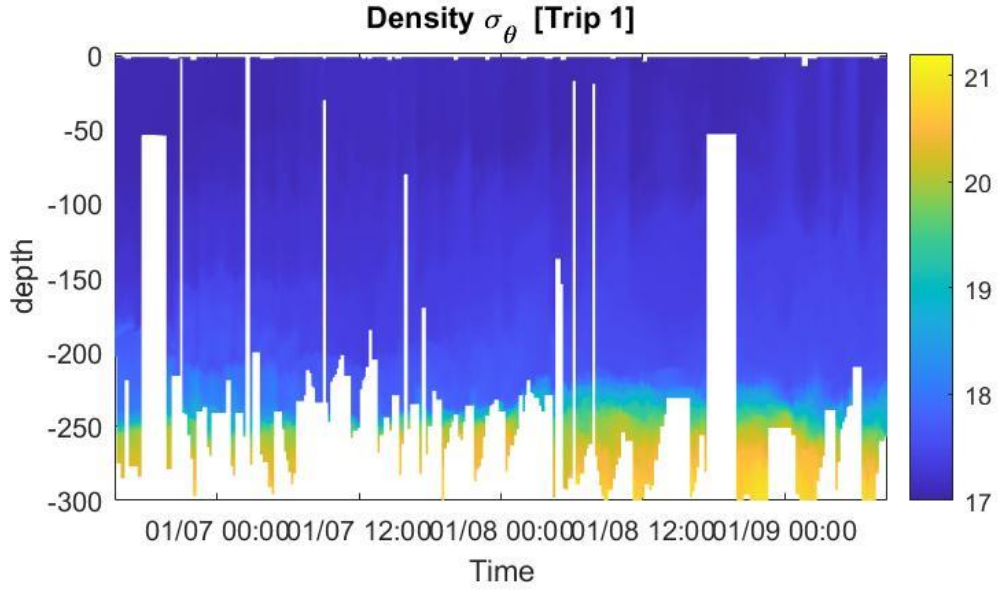

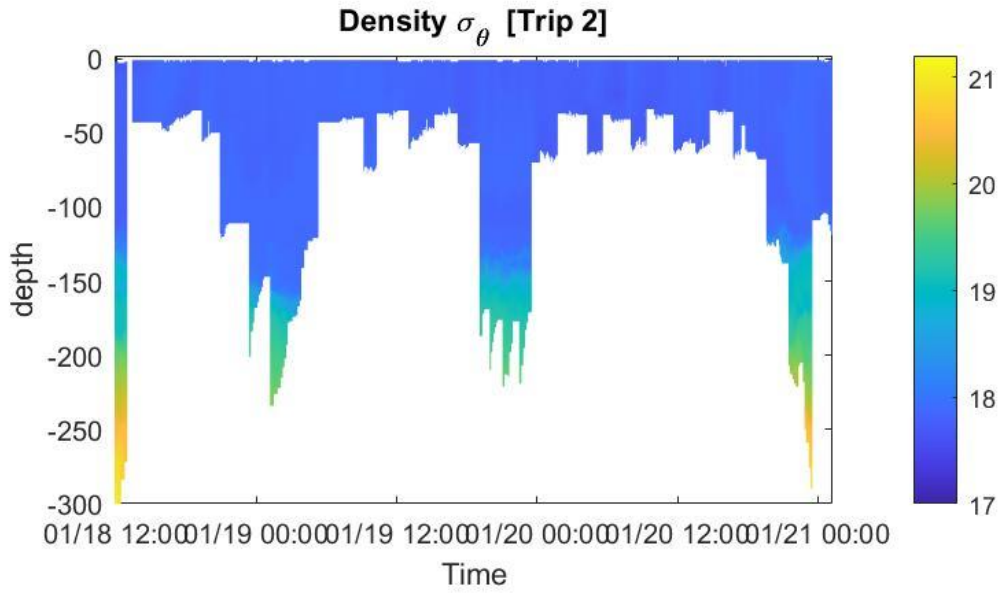

Figure 4.2 Density contours of the 2 trips in January, 2009.

According to Rosentraub (2007) in fig 4.1, the pycnoclines are about 50 meters in summer, and about 200 meters in winter. Also, the results from the two trips showed that the pycnocline has deepened to 150~ 250 meters in both trips due to downwelling. In trip 1, we observed that the pycnocline was around 250 meters, above that, the density was around 17-18 kg/m^3 in σ_θ, and beneath that, density reached 20-21 kg/m^3. In trip 2, the pycnocline was around 150 meters, where the density changes from 17-18 kg/m^3 in σ_θ to 20-21 kg/m^3. Compared with the results in the first trip, the vertical density variation is less sharp.

According to Rosentraub (2007), the northward current can reach a maximum hourly mean of 0.90 m/s in winter. The strong northward flow will create a strong onshore Ekman transport under the influence of Coriolis force. As water is being sent

ashore, pressure will be built up at the surface layer, creating the downwelling system, and deepen the pycnoclines.

As a result, at the bottom boundary layer, which was about 250-300 meters deep, the hydrographic status is distinctly different than the water mass above the pycnocline. A geostrophic offshore current is thus formed to compensate the onshore Ekman transport, transporting water downward over the shelf.

4.2 Surface mixing

In the surface layer, the magnitude of turbulent mixing is dominated by the surface forcing. The scale of turbulent mixing can be expressed as the Brunt-Väisälä buoyancy frequency N^2 in s^{-2}, and the surface forcing consisted of two components: the heat flux (fig 4.3), and the wind stress forcing (fig 4.4). The heat budget J_q^0 in W/m^2 was converted into buoyancy frequency J_b^0 in W/kg, and the wind stress forcing was presented by wind stress τ in N/m^2.

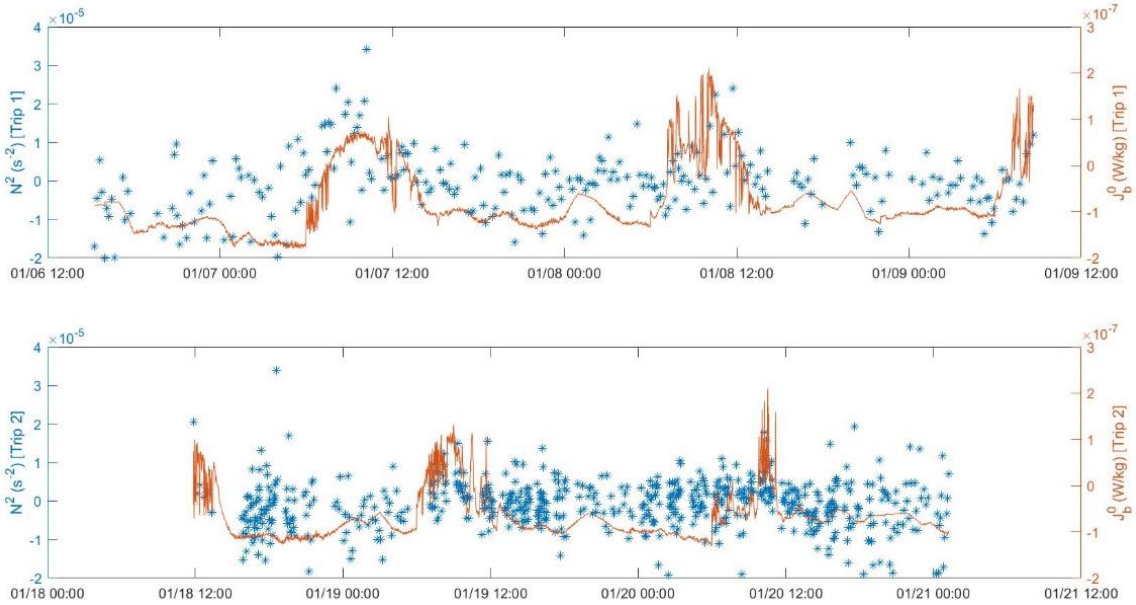

Figure 4.3 Buoyancy flux and buoyancy frequency in both trips.

As can be seen from the results of buoyancy flux and buoyancy frequency, there is a pattern between these two parameters. During daytime, with positive incoming heat flux, the seawater in the surface layer increases its temperature, and decreases the density, which leads to a more stratified environment. During night, the opposite happens due to the heat loss at the surface, which causes cooling, increasing seawater density as well as increasing the potential of convectively driven mixing. Since buoyancy flux is calculated from the heat budget, and buoyance frequency N^2 also represents the stability or stratification of the water column, which can explain the similar trend in daily variation between these two parameters.

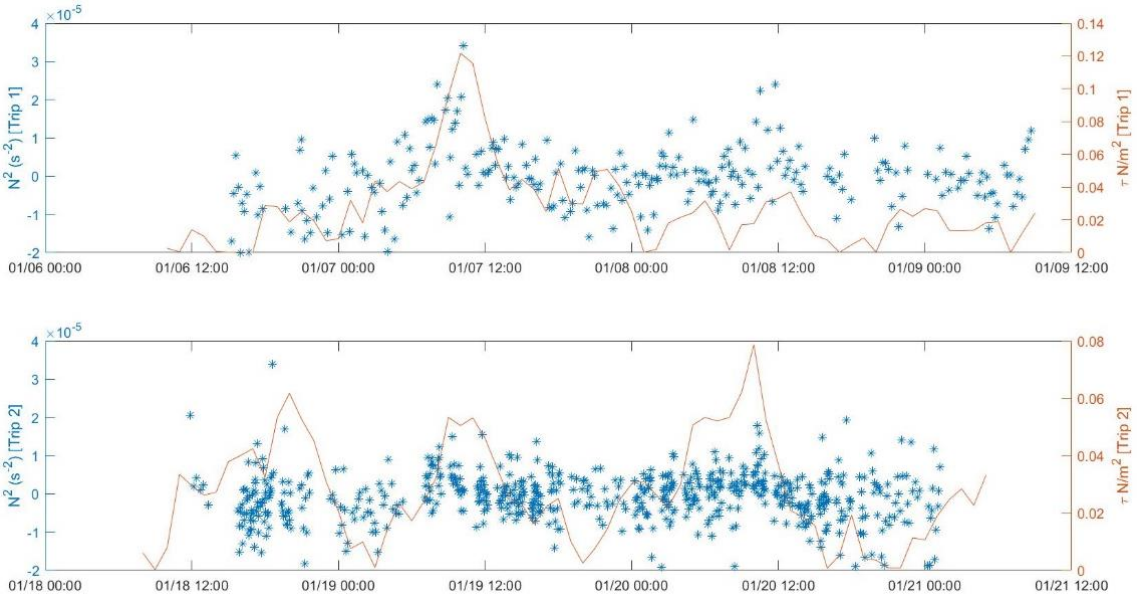

Figure 4.4 Wind stress forcing and buoyancy frequency in both trips.

However, from the comparison of wind stress forcing and buoyancy frequency, there is no clear correlation. Theoretically, the increase of wind stress could promote the mixing trend and thus decrease the buoyancy frequency. Therefore, we can make an assumption that it is the heat budget that takes the leading role of controlling the mixing and stratification trend on the surface layer in winter.

4.3 Surface mixing during night

In the night, with the heat loss due to the air-sea interaction, the seawater on the surface layer decreases in temperature and increases in density. Combined wind stress forcing, the densified water will sink and increase the turbulent mixing and the dissipation rate of TKE. The mean values and their 95% confidence intervals of surface forcing and dissipation rates within the mixing layer during each night are listed in table 4.1.

Table 4-1

Trip 1	Night 1 Jan 6	Night 2 Jan 7	Night 3 Jan 8	mean
J_q^0 (W/m^2)	'-262.6 (-265.4, -259.9)'	-202.1 (-204.9, -199.1)'	-182.2 (-184.8, -179.6)'	-216
$-J_b^0$ 10^{-7} (W/kg)	1.344 (-1.36, -1.329)'	1.061 (-1.077, -1.042)'	0.9457 (-0.9587, -0.9319)'	1.117
τ 10^{-2} (N/m^2)	2.087 (2.02, 2.155)'	3.004 (2.873, 3.136)'	1.529 (1.459, 1.599)'	2.207
M-O Length (m)	-1.676 (-1.74, -1.61)'	-3.685 (-3.859, -3.497)'	-1.523 (-1.602, -1.44)'	-2.3
D (m)	49.32 (45.67, 54.31)'	57.26 (55.53, 58.83)'	45.38 (36.88, 56.05)'	50.65
ϵ 10^{-7} (W/kg)	0.8667 (0.7366, 1.067)'	0.6415 (0.6063, 0.6796)'	2.449 (1.287, 5.827)'	1.319
Trip 2	Night 4 Jan 18	Night 5 Jan 19	Night 6 Jan 20	mean
J_q^0 (W/m^2)	-187.7 (-190.2, -185.1)'	-172.7 (-174.7, -170.7)'	-147.6 (-150, -145.7)'	-169
$-J_b^0$ 10^{-7} (W/kg)	0.9868 (-1, -0.9717)'	0.8986 (-0.9097, -0.8877)'	0.7335 (-0.7456, -0.7229)'	0.873
τ 10^{-2} (N/m^2)	3.361 (3.2, 3.503)'	1.941 (1.872, 2.008)'	1.114 (1.052, 1.182)'	2.139
M-O Length (m)	-4.692 (-4.915, -4.437)'	-2.256 (-2.354, -2.164)'	-0.8065 (-0.8679, -0.7495)'	-2.59
D (m)	37.83 (32.58, 43.44)'	37.63 (34.29, 41.14)'	40.12 (34.98, 46.27)'	38.53
ϵ 10^{-7} (W/kg)	426.4 (246.2, 662.5)'	31.11 (11.92, 88.16)'	3.432 (1.805, 6.118)'	153.6

Table 4.1. Mean values and 95% confidence intervals for each night, Night 1, 2, 3 is on Jan. 6, 7, and 8 from trip 1, and Night 4, 5, 6 is on Jan. 18, 19, and 20 from trip 2. J_q^0 is (negative during night representing heat loss); $-J_b^0$ is the buoyancy flux; τ is the wind stress; M-O (Monin-Obukhov) Length is the ratio between surface wind forcing and buoyancy flux. D is the mixed layer depth, and ϵ is the TKE dissipation rate within the mixed layer.

As can be seen from the results, in trip 1, the buoyancy flux is on the order of 10^{-7} W/kg, the wind stress is about 0.02 N/m^2, and the dissipation rate ϵ has a similar order of magnitude to that of the buoyancy flux. The mixed layer depth is about 50 meters, and the M-O length round ~2.3 meters, which means the turbulent mixing in the upper 2.3 meter was likely dominated by wind stress forcing, while being controlled by surface buoyancy flux beneath 2.3 meters. During the second night, the wind stress peaks at 0.03 N/m^2, which allowed the impact of the winds stress to penetrate slightly deeper, to 3.6

meters. For trip 2, the mixed layer depth is about 38 meters, and the M-O length round ~2.6 meters, which is slightly deeper than that in trip 1 by 0.3 meters, indicating a larger impact from wind forcing on average.

For trip 2, we found that the first two nights had abnormally high values of dissipation rate, which is caused by the storm before the trip (fig 4.5). As can be seen from the observed wind speed data in Hadera station, there is a storm took place in this region several days before trip 2 on Jan 14. The storm with a maximum wind speed of 10 m/s can stir the sea surface, increase the wave condition and causing wave breaks with significant levels, which cannot take place under regular wind condition, which eventually increase the turbulent mixing and the dissipation rate of TKE dramatically (Terray et al. 1996). After the storm, the surface layer is sufficiently well mixed and the dissipation rate will decrease gradually and back to a normal status in several days.

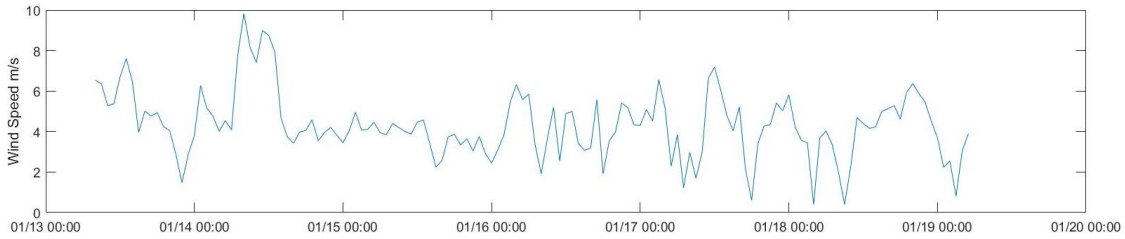

Figure 4.5 Wind speed data from Hadera station.

To better understand the general connection between ϵ and J_b^0, ϵ/J_b^0 were plotted against z/D, which is the depth over the mixing layer depth. Since ϵ and J_b^0 share the same unit of W/kg, and z and D are both depths, by using ϵ/J_b^0 against z/D, we can convert all the data into non-dimension numbers to remove the differences in mixing layer depth and buoyancy flux between each profile.

From the profiles of ϵ/J_b^0, we can find that in all nights, the value is decreasing with the depth, because the decay of buoyancy flux and wind stress forcing. In the mixed layer, in trip 1, the ϵ/J_b^0 is around 1, and in trip 2, the values are about 500 and 20 in the first and second night. In all 3 nights in trip 1, the ϵ/J_b^0 profiles is decreasing dramatically from the surface to the depth where z/D = -0.4, and beneath that, ϵ/J_b^0 value stays around 0.5 from the z/D = -0.4 to the mixing layer depth. In Night 4, ϵ/J_b^0 value starts around 1000 in the surface and decrease with depth to around 100 at z/D = -0.6, and beneath that, ϵ/J_b^0 value stays around 100 from the z/D = -0.6 to the mixing layer depth. Similar trends can also be found in Night 5 and Night 6, but with a different order of magnitude. Beneath the mixed layer (z/D = -1), the value of ϵ/J_b^0 drops to a level less than 1 in all 6 nights, which indicates that even the influence of the storm on turbulent mixing can increase the TKE dissipation rate within the mixing layer by 10~100 times, and persist for several days, however it cannot penetrate the mixing layer.

In Anis (1994), a similar study was applied to the ocean boundary layer of Pacific Ocean between March 13 and 20 in 1987, and the results of ϵ/J_b^0 share a similar trend to results from trip 1. The ϵ/J_b^0 decreases largely to about 0.5 at z/D is ~-0.5, it decreases gradually until the mixing layer depth, and it decreases to almost 0 beneath that.

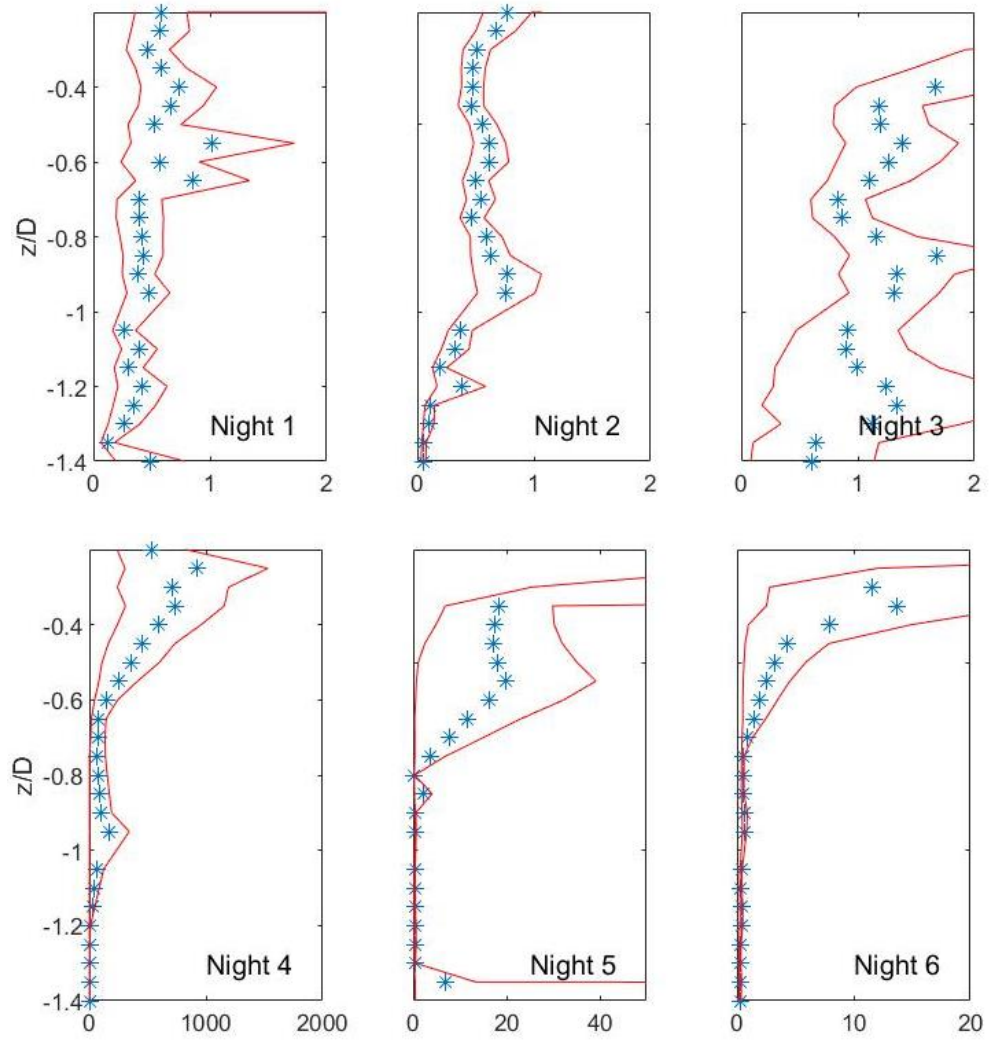

Figure 4.6 Profiles of averaged ϵ/J_b^0 during each night. The results are plotted against the depth over the mixing layer depth to remove the influence of the mixing layer depth. The dots represent the actual value and the dashed line stands for 95% confidence from the bootstrap method.

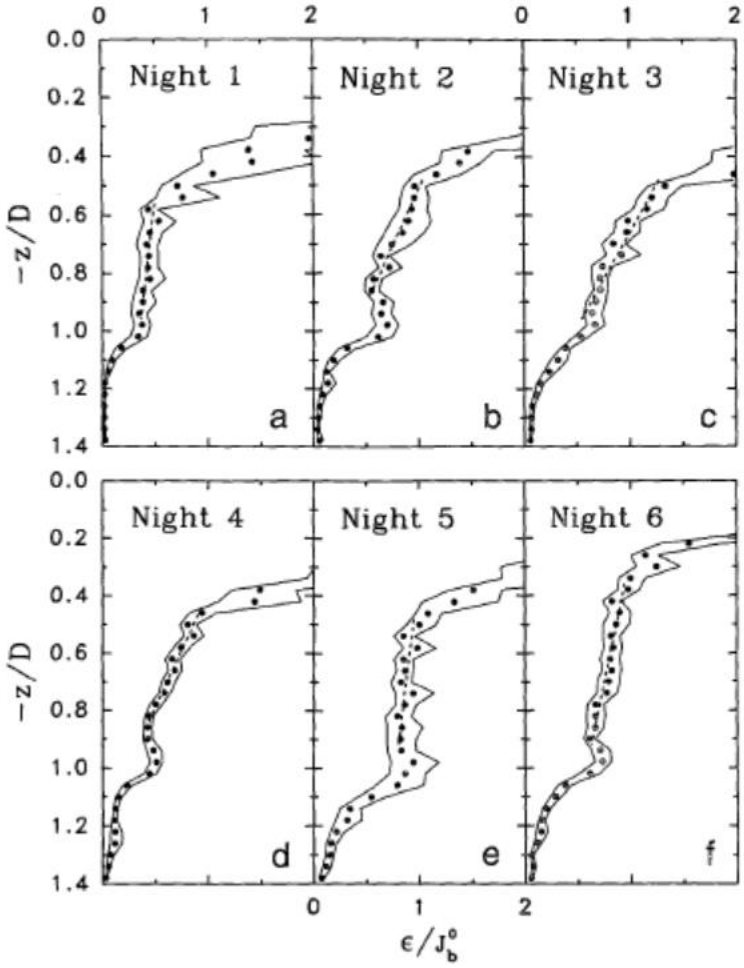

Figure 4.7 Profiles of averaged ϵ/J_b^0 during each night from fig. 3in Anis (1987). The dots represent the actual value and the dashed line stands for 95% confidence from the bootstrap method. (© American Meteorological Society**)**

4.4 Buoyancy frequency and the dissipation rate

The averaged results for all night profiles from 2 trips of the buoyancy frequency and dissipation rate are plotted and compared. For N^2, the values decrease from the surface, and stays negative from z/D = 0.2 to the mixing layer depth. Beneath that, the buoyancy frequency peaks again at the mixing layer depth. The buoyancy frequency represents the level of stratification, which is strong at the most surface layer due to the

air-sea interaction and around the mixing layer depth, where the pycnocline provide strong vertical density gradient.

The negative value of the buoyancy frequency represents the instability of the water column, which indicates higher turbulent mixing. By comparing with the results from trip 1, the results from trip 2 have a less order of magnitude, and within the mixed layer, the buoyancy frequency is basically negative, both of which are probably due to the strong mixing brought by the storm.

For the dissipation rate, in trip 1 it decreases dramatically from the magnitude of 10^{-5} W/kg on the surface to about 10^{-7} W/kg where z/D=-0.4, however, in trip 2 it begins with 10^{-4} W/kg and falls to 10^{-5} W/kg where z/D=-0.6. In both trips, the dissipation rate stays at the same value until the mixing layer depth, and beneath that, the dissipation rate of the turbulent kinetic energy declines again and stays around 10^{-8} W/kg.

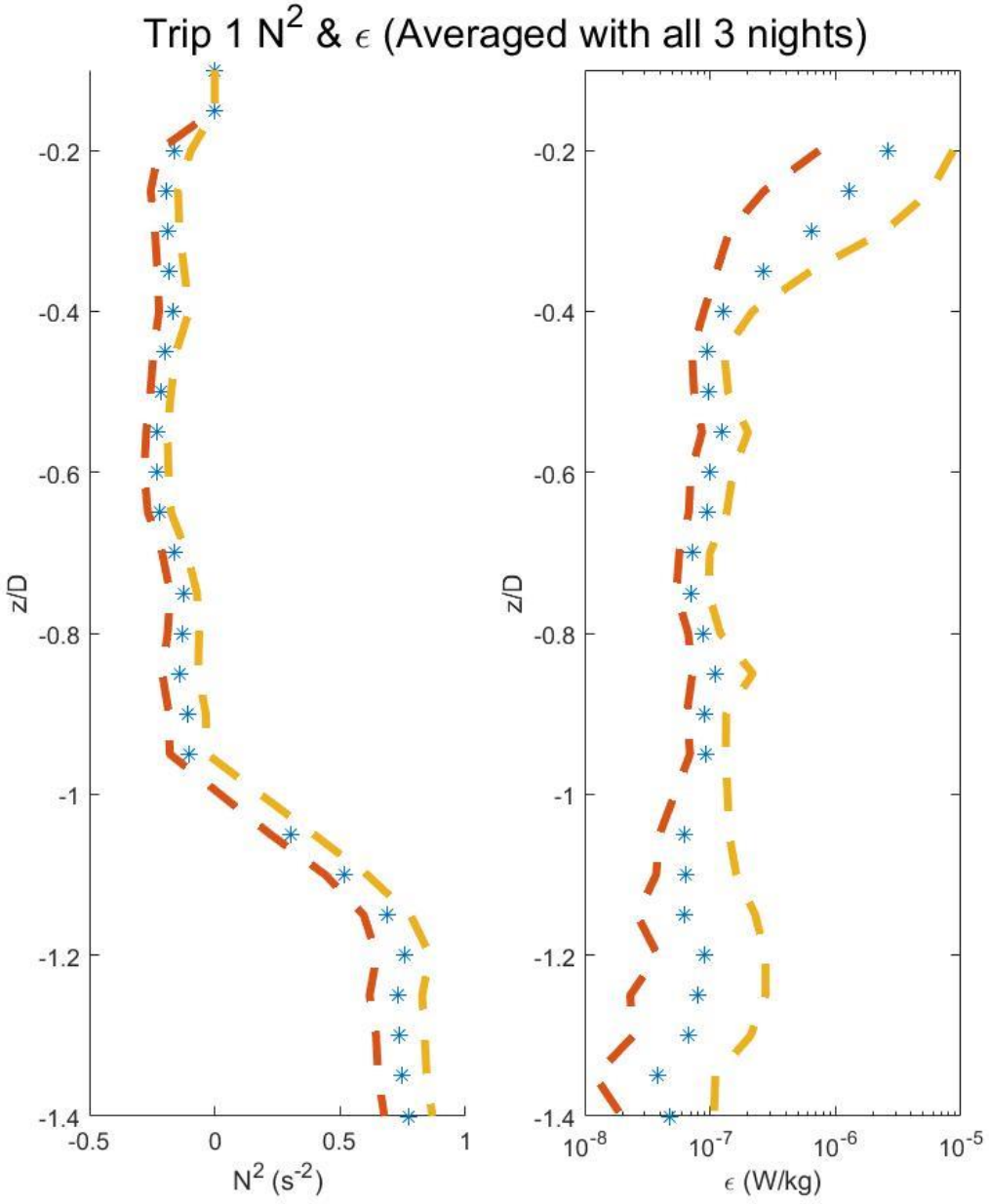
Trip 1 N^2 & ϵ (Averaged with all 3 nights)
z/D
-0.2
-0.4
-0.6
-0.8
-1
-1.2
-1.4
-0.5
0
0.5
1
N^2 (s^{-2})
10^{-8}
10^{-7}
10^{-6}
10^{-5}
ϵ (W/kg)

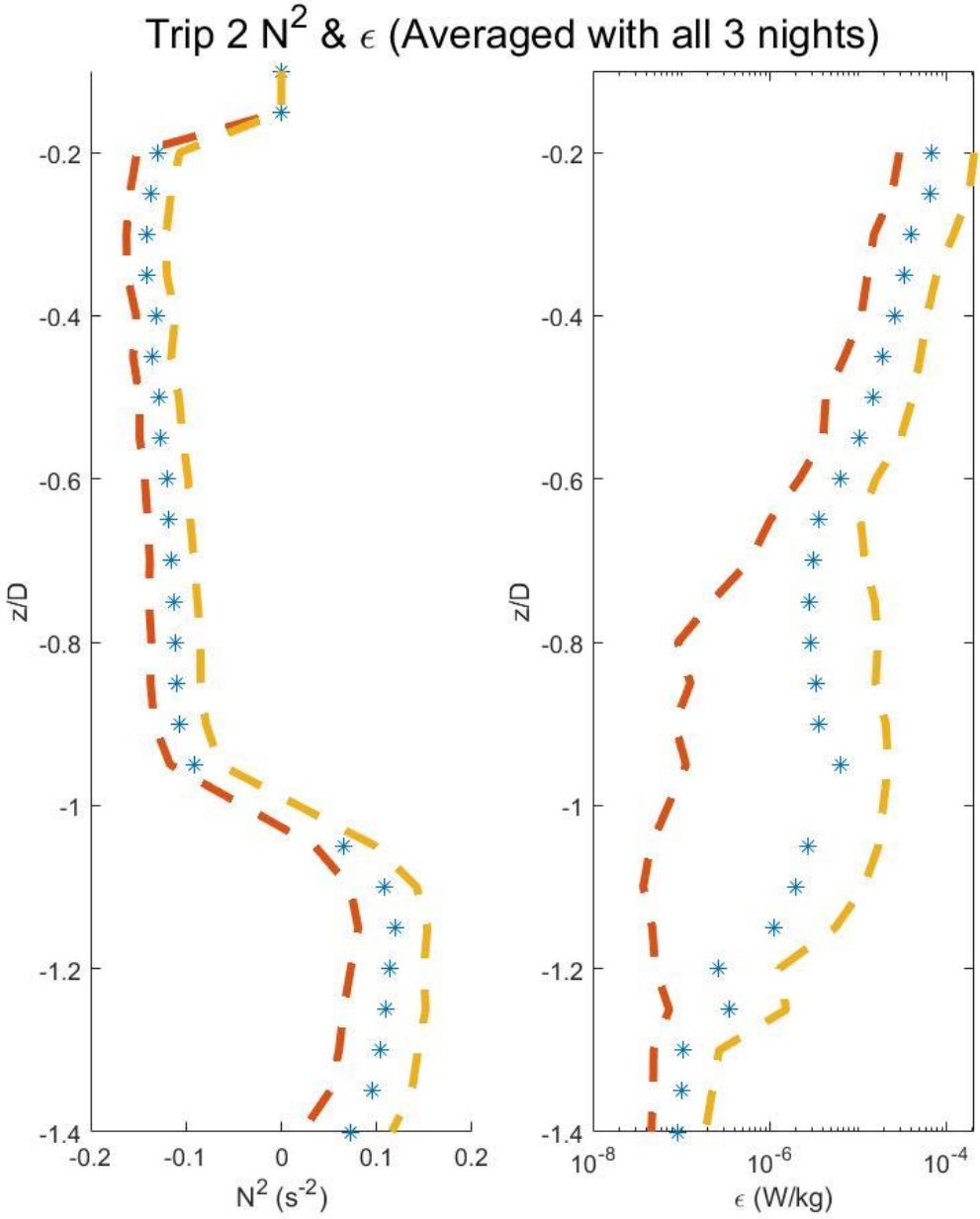

Figure 4.8 Profiles of the averaged buoyancy frequency and the dissipation rate for each trip (upper: trip 1; lower: trip 2). The results are plotted against the depth over the mixing layer depth to remove the influence of the mixing layer depth. The dots represent the actual value and the dashed line stands for 95% confidence from the bootstrap method.

4.5 Similar studies

The dissipation rate of the turbulent kinetic energy is an important parameter for turbulence study. Therefore, it has been calculated and analyzed with varies methods.

According to Moum (1995), 1000 microstructure profiles from 2 different trips with different measurement and methods were compared. From the results in this study, the distribution of the dissipation rate presents a similar trend as the results in this study. The dissipation rate was around 10-7 in the surface and dropped dramatically to 10-9 beneath the mixed layer depth.

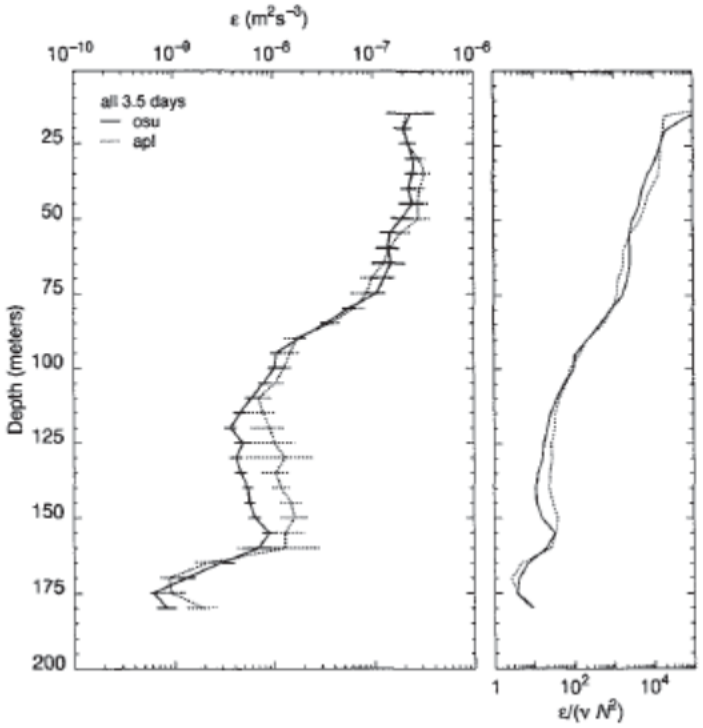

Figure 4.9 Turbulent kinetic energy data from Figure 1 in Moum (1995). (© American Meteorological Society**)**

However, this method of estimating the dissipation rate from the velocity shear data also have its limitation. According to Scheifele (2018), a case study was conducted in the Arctic Ocean, which is dominated by a strongly stratified environment with low turbulent kinetic energy. The dissipation rate derived from the velocity shear with Nasmyth spectrum and that derived from temperature data have large disagreements. This suggests that the dissipation rate from the shear methods is not accurate enough in an environment with low mixing events and low turbulent kinetic energy. However, in our study, this method is still effective, since the mixing in the Israel Shelf in winter is strong enough.

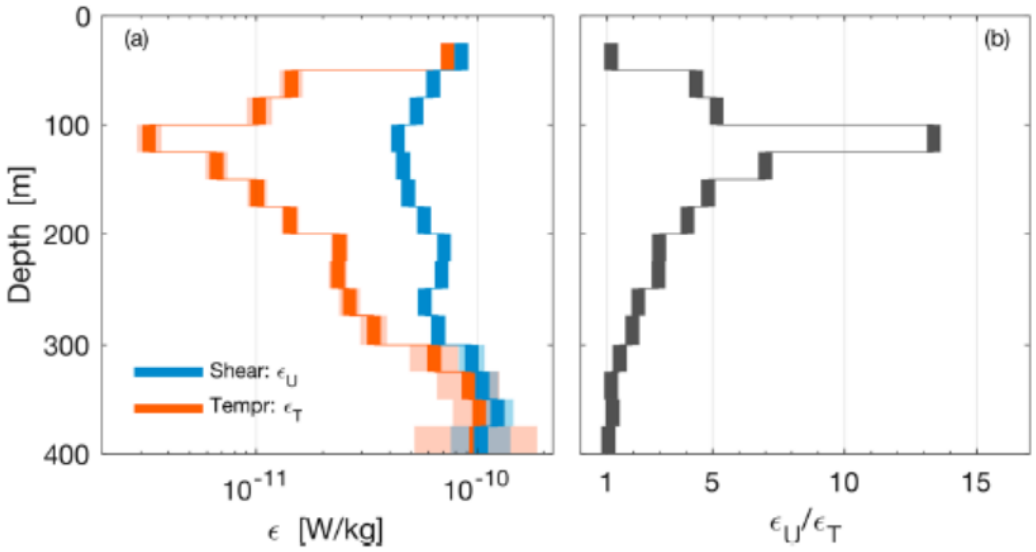

Figure 4.10 TKE dissipation rate data obtained in Figure 4 of Scheifele (2018). The dissipation rate derived from the velocity shear (blue) and that derived from temperature data (orange) demonstrated large disagreements.

5. CONCLUSION

This research studied the winter turbulent mixing status across the Israeli shelf in the southeast Mediterranean Sea. The hydrological observation data was obtained during two research cruises in the central Israeli Shelf in 2009 January 6th-9th and 18th-21st. Observed meteorological data is from the stations of Hadera, Maabarot, Hamaapil, R/V Shikmona, as well as from ERA-5 reanalysis data of ECMWF.

The dissipation rate of turbulent kinetic energy was estimated from the Nasmyth spectrum fitting of microstructure velocity shear data. Buoyancy flux was calculated from the heat budget components which included the short-wave radiation, long-wave radiation, sensible heat flux, and latent heat flux. The surface friction velocity was calculated from the wind speed data of Hadera station. The buoyancy frequency was calculated from the hydrological observation data obtained by two trips with R/V Shikmona.

The water column in the studied area was dominated by a downwelling system under the Ekman transport forced by northward wind stress. On the surface layer, the turbulent mixing is under the impact of both wind stress and buoyancy flux. The wind can transfer kinetic energy into the sea surface, and surface cooling from negative heat budget can densify the surface water resulting in instability of the water column. After comparing the buoyancy frequency, buoyancy flux Jb0, and friction velocity u*, the buoyancy flux appears to have had a larger influence on the turbulent mixing during nighttime.

As can been seen from the results in trip 2, it might be that the storm that stirred the surface, made the surface water column sufficiently well mixed, and increase the dissipation rate by transferring more turbulent kinetic energy into the water column through wave breaking. By comparing the averaged results from all three nights in both trips, the impact of the storm tends to influence deeper within the mixing layer, but cannot penetrate the mixing layer depth.

The scale of the turbulent mixing can be presented by the dissipation rate of turbulent kinetic energy, and with more sufficient turbulent mixing, the dissipation rate will also be higher. Within the mixed layer, the averaged dissipation rate is about 10^{-7} W/kg, which drops from 10^{-5} to 10^{-8} from the surface to the mixing layer depth. On the other hand, the buoyancy frequency represents the level of stratification. From the surface layer, the buoyancy frequency first decreases with depth and increases again as approaching to the mixing layer depth. At the mixing layer depth, the buoyancy frequency peaks due to the high vertical density gradient from pycnoclines.

Future work

This thesis discussed the turbulent mixing on the surface of Israel shelf in winter time, and in the meantime, the friction between the benthic and the off-shore bottom current can also increase the turbulent mixing in the bottom boundary current. To better understand the turbulent mixing at the bottom, more accurate velocity and CTD sensor should be deployed at the relating depth.

Storms with strong winds are common in winter, which can increase the level of turbulent mixing, transfer more turbulent kinetic energy into the water column through breaking waves, and thus increase the dissipation rate. It might be important to look deeper at the impact of storms to the surface turbulent mixing. Also, in the summer, when the wind become southward, the water column will be dominated by an upwelling system with much shallower pycnoclines, and the status of the turbulent mixing could be much different than that in winter.

6. REFERENCE

Abudaya, Mohammed. "Seasonal and spatial variation in sea surface temperature in the South-East Mediterranean Sea." (2013).

Anis, A., & Moum, J. N. (1994). Prescriptions for heat flux and entrainment rates in the upper ocean during convection. Journal of physical oceanography, 24(10), 2142-2155.

Anis, A., Singhal, G., Mixing in the surface boundary layer of a tropical freshwater reservoir, Journal of Marine Systems, Volume 63, Issues 3–4, 2006, Pages 225-243, ISSN 0924-7963, https://doi.org/10.1016/j.jmarsys.2006.07.003.

Bryant, Kyra M., and Muhammad Akbar. 2016. "An Exploration of Wind Stress Calculation Techniques in Hurricane Storm Surge Modeling" Journal of Marine Science and Engineering 4, no. 3: 58. https://doi.org/10.3390/jmse4030058

Elena Jurado, José-Manuel Zaldívar, Dimitar Marinov, Jordi Dachs, Fate of persistent organic pollutants in the water column: Does turbulent mixing matter?, Marine Pollution Bulletin, Volume 54, Issue 4, 2007, Pages 441-451, ISSN 0025-326X, https://doi.org/10.1016/j.marpolbul.2006.11.028.

Fer, I., Skogseth, R., & Geyer, F. (2010). Internal Waves and Mixing in the Marginal Ice Zone near the Yermak Plateau, Journal of Physical Oceanography, 40(7), 1613-1630. Retrieved Jul 23, 2021, from https://journals.ametsoc.org/view/journals/phoc/40/7/2010jpo4371.1.xml

Foken, T. 50 Years of the Monin–Obukhov Similarity Theory. Boundary-Layer Meteorol 119, 431–447 (2006). https://doi.org/10.1007/s10546-006-9048-6

Forryan, A., et al. "Turbulent mixing in the eddy transport of Western Mediterranean Intermediate Water to the Alboran Sea." Journal of Geophysical Research: Oceans 117.C9 (2012).

Herut, B., Almogi-Labin, A., Jannink, N., & Gertman, I. (2000). The seasonal dynamics of nutrient and chlorophyll a concentrations on the SE Mediterranean shelf-slope. Oceanologica Acta, 23(7), 771-782.

Klein, P., & Coantic, M. (1981). A numerical study of turbulent processes in the marine upper layers. Journal of Physical Oceanography, 11(6), 849-863.

Lueck, R. G. "RSI Technical Note 030 On the Forms of the Velocity." Shear, and Rate-of-Strain Spectra (2014): 1-5.

Lueck, R. G. "RSI technical note 028 Calculating the rate of dissipation of turbulent kinetic energy." Victoria, BC, Canada: Rockland Scientific International. Retrieved from http://rocklandscientific. com/support/knowledge-base/technical-notes (2016).

Malanotterizzoli, P., and A. Hecht. "Large-scale properties of the eastern mediterranean-A review." Oceanologica Acta 11.4 (1988): 323-335.

Menzin, A. B., and L. V. Moskalenko. "Calculation of wind driven currents in the Mediterranean Sea by the electrical simulation method." Oceanologica 22 (1982): 537-540.

Moum, J. N., Gregg, M. C., Lien, R. C., & Carr, M. E. (1995). Comparison of turbulence kinetic energy dissipation rate estimates from two ocean microstructure profilers. Journal of Atmospheric and Oceanic Technology, 12(2), 346-366.

Nasmyth, P. W. (1970). Oceanic turbulence (Doctoral dissertation, University of British Columbia).

Oakey, N. S. (1982). Determination of the Rate of Dissipation of Turbulent Energy from Simultaneous Temperature and Velocity Shear Microstructure Measurements, Journal of Physical Oceanography, 12(3), 256-271. Retrieved Jul 5, 2021, from https://journals.ametsoc.org/view/journals/phoc/12/3/1520-0485_1982_012_0256_dotrod_2_0_co_2.xml

Price, J. F., Weller, R. A., & Schudlich, R. R. (1987). Wind-driven ocean currents and Ekman transport. Science, 238(4833), 1534-1538.

Robinson, A. R., Malanotte-Rizzoli, P., Hecht, A., Michelato, A., Roether, W., Theocharis, A., ... & Osman, M. (1992). General circulation of the Eastern Mediterranean. Earth-Science Reviews, 32(4), 285-309.

Robinson, A. R., Golnaraghi, M., Leslie, W. G., Artegiani, A., Hecht, A., Lazzoni, E., ... & Ünlüata, Ü. (1991). The eastern Mediterranean general circulation: features, structure and variability. Dynamics of Atmospheres and Oceans, 15(3-5), 215-240.

Rosentraub, Z., and Brenner, S. (2007), Circulation over the southeastern continental shelf and slope of the Mediterranean Sea: Direct current measurements, winds, and numerical model simulations, J. Geophys. Res., 112, C11001, doi:10.1029/2006JC003775.

S. A. Thorpe, An Introduction to Ocean Turbulence, Cambridge University Press, 2007.

Scheifele, B., Waterman, S., Merckelbach, L., & Carpenter, J. R. (2018). Measuring the dissipation rate of turbulent kinetic energy in strongly stratified, low‐energy

environments: A case study from the Arctic Ocean. Journal of Geophysical Research: Oceans, 123(8), 5459-5480.

Thiébaut, M., Filipot, J. F., Maisondieu, C., Damblans, G., Duarte, R., Droniou, E., & Guillou, S. (2020). Assessing the turbulent kinetic energy budget in an energetic tidal flow from measurements of coupled ADCPs. Philosophical Transactions of the Royal Society A, 378(2178), 20190496.

Wiles, P. J., Rippeth, T. P., Simpson, J. H., & Hendricks, P. J. (2006). A novel technique for measuring the rate of turbulent dissipation in the marine environment. Geophysical Research Letters, 33(21).